

WHAT ARE “X-SHAPED” RADIO SOURCES TELLING US?

I. VERY LARGE ARRAY IMAGING OF A LARGE SAMPLE OF LOW AXIAL RATIO RADIO SOURCES

David H. Roberts

Department of Physics MS-057, Brandeis University, Waltham, MA 02453-0911, USA

Lakshmi Saripalli

Raman Research Institute, C. V. Raman Avenue, Sadashivanagar, Bangalore 560080, India

Kevin X. Wang

Department of Physics MS-057, Brandeis University, Waltham, MA 02453-0911, USA

Mayuri Sathyanarayana Rao & Ravi Subrahmanyam

Raman Research Institute, C. V. Raman Avenue, Sadashivanagar, Bangalore 560080, India

Carly C. KleinStern, Christopher Y. Morii-Sciolla, & Liana Simpson

Department of Physics MS-057, Brandeis University, Waltham, MA 02453-0911, USA

`roberts@brandeis.edu, lsarapal@rri.res.in`

ABSTRACT

We present historical VLA and Jansky Very Large Array multi-frequency multi-array radio continuum imaging of a unique sample of 100 radio sources that have been selected on the basis of low axial ratios. These observations allow us the opportunity to study radio sources with synchrotron plasma that is significantly offset from the main radio axis and therefore open a window into investigations of physical mechanisms responsible for depositing the plasma in off-axis regions. These images are discussed in detail in subsequent papers in this series (Saripalli & Roberts 2017; Roberts & Saripalli 2017).

Subject headings: black holes — galaxies: active — radio continuum: galaxies

Version of August 7, 2017.

1. INTRODUCTION

The “X-shaped” radio galaxies (XRGs) are of intense interest because one possible scenario for their formation involves pairs of supermassive black holes (SMBHs). Such pairs are presumed to be the natural results of galaxy mergers (Begelman, Blandford, & Rees 1980). This led Merritt & Ekers (2002) to suggest that XRGs were signposts for SMBH pairs. Since the coalescence of SMBH pairs is thought to be the leading source of the low-frequency gravitational wave background, their statistics can give us a handle on the rate of such events. In Roberts et al. (2015), henceforth Paper I, we presented the beginning of our study of XRGs, archival VLA imaging of a subsample of 100 candidate XRGs selected by Cheung (2007). There we showed images of 52 of the candidates, and discussed the various morphologies that we found. We concluded in Roberts, Saripalli, & Subrahmanyam (2015) that the rate of formation of binary SMBHs may have been previously overestimated by a factor of 3-5.

In this paper we present Jansky Very Large Array multi-frequency multi-array observations of 86 radio galaxies and quasars out of the Cheung (2007) sample (the rest were missed due to insufficient observing time). Including the archival data presented by Roberts et al. (2015), we made images of 95/100 of the candidate XRGs. Subsequent papers in this series discuss the results in detail (Saripalli & Roberts 2017; Roberts & Saripalli 2017).

The next section gives details of the observations and imaging methods. Section 3 presents the results, followed by a summary in Section 4.

2. OBSERVATIONS

We observed the Cheung (2007) sample of sources from 2016 February 04 through 2017 January 10 using the NRAO Jansky Very Large Array at L- (1.4 GHz) and S-bands (3 GHz) and the A, B, and C-arrays (one epoch was in the transitional AB-array). Each source was observed in a single snapshot that ranged from about 180 to about 240 seconds duration, depending on scheduling constraints. At S band we used 16 spectral windows of 128 MHz with a net average frequency of about 3 GHz, while at L-band we used 16 spectral windows of 64 MHz width, with an average frequency of between 1.4 and 1.6 GHz, depending on the flagged spectral windows. The spectral windows were each divided into 64 channels. Each data set was edited for interference by the pipeline (see below) and then inspected by hand, with a typical loss of a few of the spectral windows. The log of our observations is given in Table 1. All-in-all we had data from both archival VLA data (Roberts et al. 2015) and Jansky VLA data on 46 sources, archival data only on six, Jansky VLA data only on

43, and a total of five sources were missed altogether.

Although JVLA observations were proposed for the full sample of 99 sources (one source was found to be of head-tail nature based on the archival data in Roberts et al. (2015)), we could observe only a subset of sources in each of the arrays because of the “C” priority assigned to most of the granted observing time. The data were analyzed at Brandeis University. We used our own version of the CASA (McMullin et al. 2007) data calibration pipeline package which we edited to add polarization calibration. Total intensity, spectral index, and complex polarization images were made of every source-frequency-array combination using multifrequency synthesis (Rao & Cornwell 2011) in CASA. Where possible the images were self-calibrated in CASA using a Python script to do the bookkeeping (Harrison 2014).¹

3. RESULTS

Radio images for all of the sources are presented in sets of nine in Figures 1–27. For each source the various images are presented in order of increasing angular resolution–S-band C-array, L/B, S/B, C/B, and L/A. The lowest contour level and peak for each image are presented in Table 2. In every plot the contour levels increase by successive factors of $2^{1/2}$. Where we had both archival and JVLA images at L-band in the A-array we present only the JVLA image; otherwise we present the archival image (see Table 1). Optical overlays using the Sloan Digital Sky Survey (DR12) r-band images are presented in Figures 28–38; for each source we used what we judged to be the best VLA image. In a few cases SDSS images were not available, and there we used the USNO Image and Catalog Archive Server (<http://www.usno.navy.mil/USNO/astrometry/optical-IR-prod/icas>) to find suitable optical images.

4. SUMMARY

In this paper we have presented Jansky Very Large Array multi-band multi-array continuum imaging of a unique sample of 100 radio galaxies that have been selected on the basis of low axial ratios. In our next paper we select a sample of 87 for study, thoroughly characterize their morphologies, and present scenario for their formation (Saripalli & Roberts 2017). In Roberts & Saripalli (2017) we discuss the sources that show clear evidence of black hole axis precession. ? uses polarization and spectral index information to examine models

¹The self-calibration script emulates the flow of the Caltech program DIFMAP; it is available from D.H.R.

for the formation of the structure of radio galaxies with significant off-axis emission.

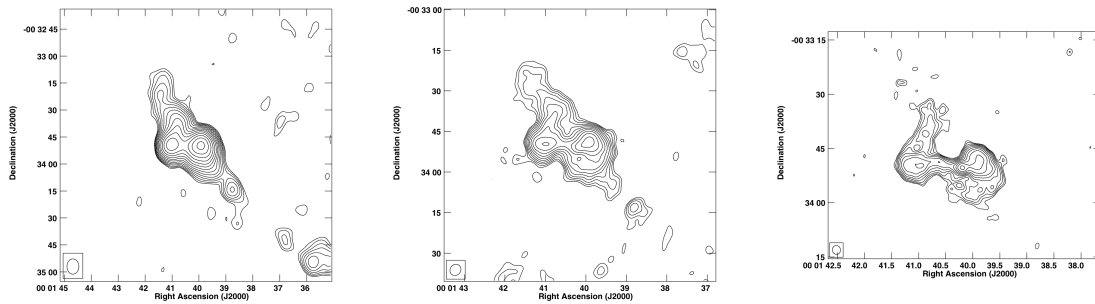
In the future we will also be deriving radio-optical relationships for those sources for which suitable images of the host galaxies exist. We also intend to obtain more complete optical information on the host galaxies by carrying out comprehensive radio-optical studies for the sample.

5. ACKNOWLEDGMENTS

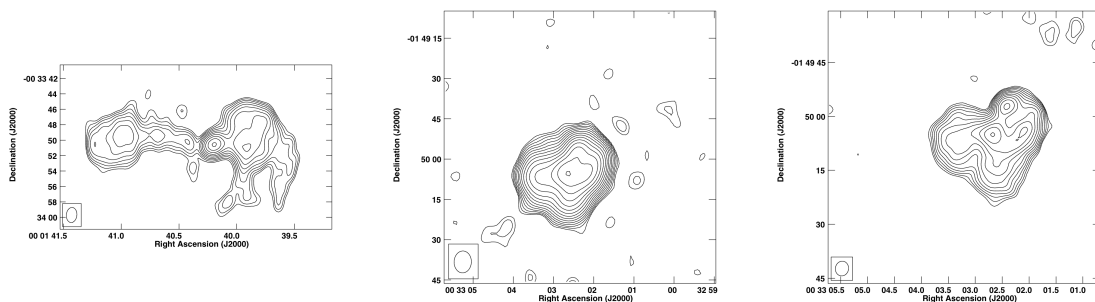
The National Radio Astronomy Observatory is a facility of the National Science Foundation, operated under cooperative agreement by Associated Universities, Inc. Funding for the Sloan Digital Sky Survey IV has been provided by the Alfred P. Sloan Foundation, the U.S. Department of Energy Office of Science, and the Participating Institutions. SDSS-IV acknowledges support and resources from the Center for High-Performance Computing at the University of Utah. The SDSS web site is www.sdss.org. D. H. R. gratefully acknowledges the support of the William R. Kenan, Jr. Charitable Trust. We thank Rachel Harrison for her CASA self-calibration script.

Facilities: Historical VLA Data Archive (see Paper I); Jansky VLA (VLA 16A-220, 16B-023).

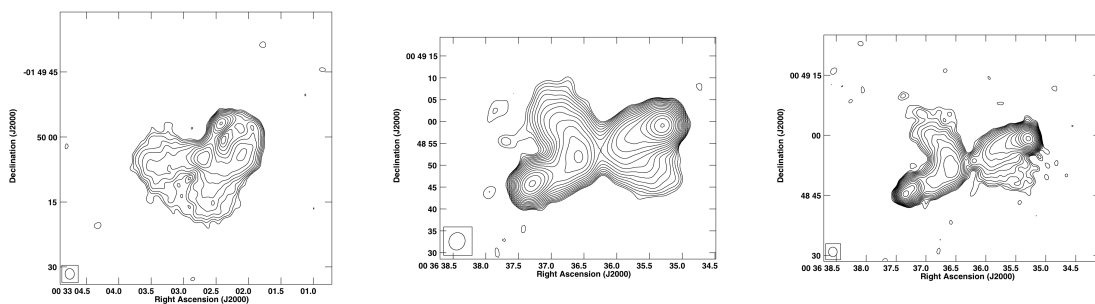
6. APPENDIX—ALL OF THE IMAGES



(a) J0001–0033, C-array S-band.(b) J0001–0033, B-array L-band.(c) J0001–0033, B-array S-band.

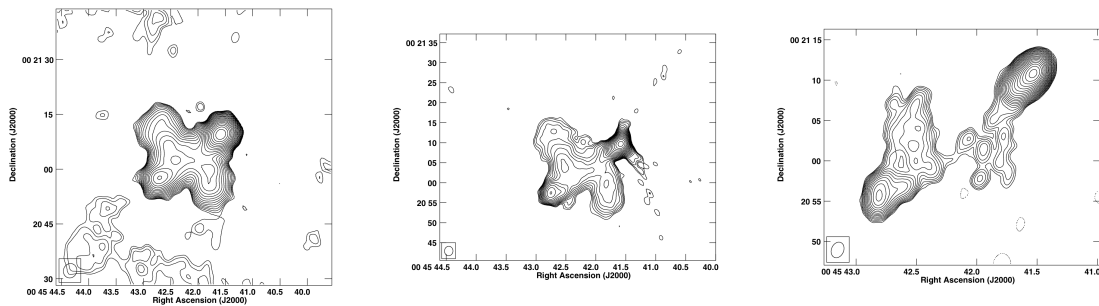


(d) J0001–0033, A-array L-band.(e) J0033–0149, C-array S-band.(f) J0033–0149, B-array L-band.

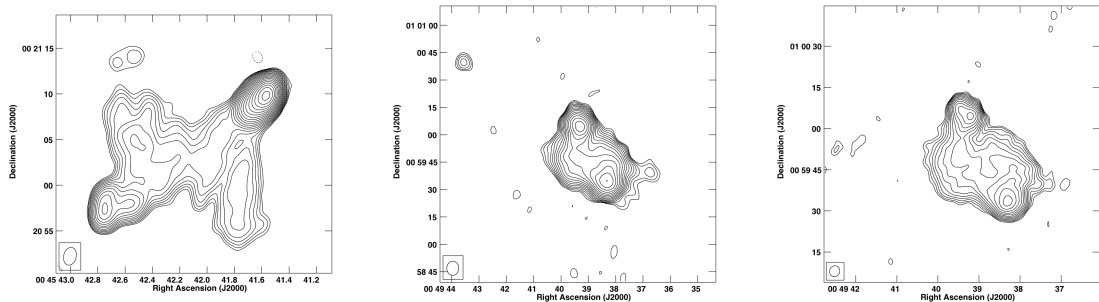


(g) J0033–0149, B-array S-band.(h) J0036+0048, B-array L-band. (i) J0036+0048, B-array S-band.

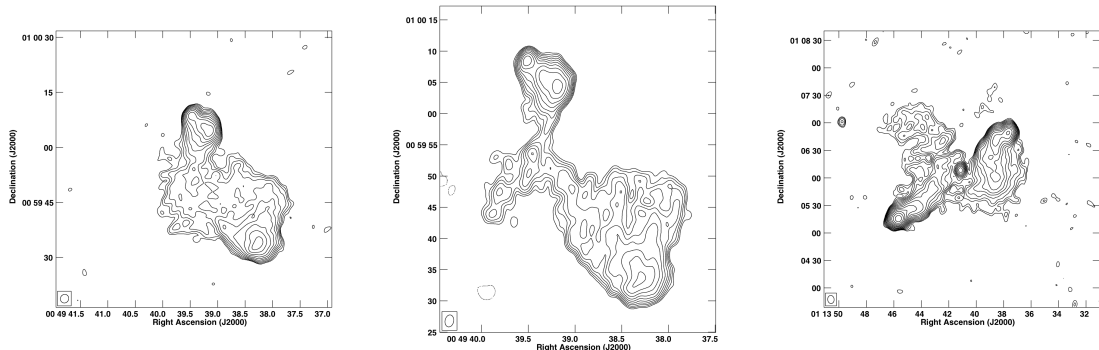
Fig. 1.—: VLA images of a sample of 100 low axial ratio radio sources (1/27).



(a) J0045+0021, B-array L-band.(b) J0045+0021, B-array S-band.(c) J0045+0021, B-array C-band.



(d) J0045+0021, A-array L-band.(e) J0049+0059, C-array S-band.(f) J0049+0059, B-array L-band.



(g) J0049+0059, B-array S-band.(h) J0049+0059, A-array L-band.(i) J0113+0106, C-array S-band.

Fig. 2.—: VLA images of a sample of 100 low axial ratio radio sources (2/27).

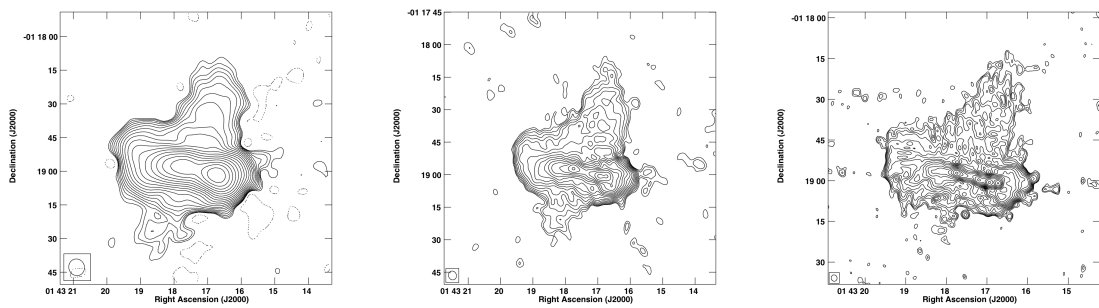
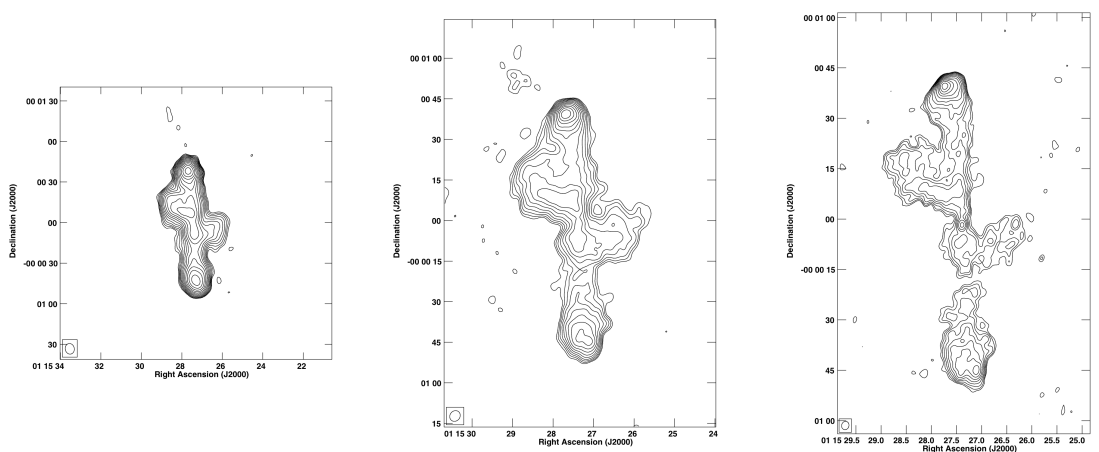
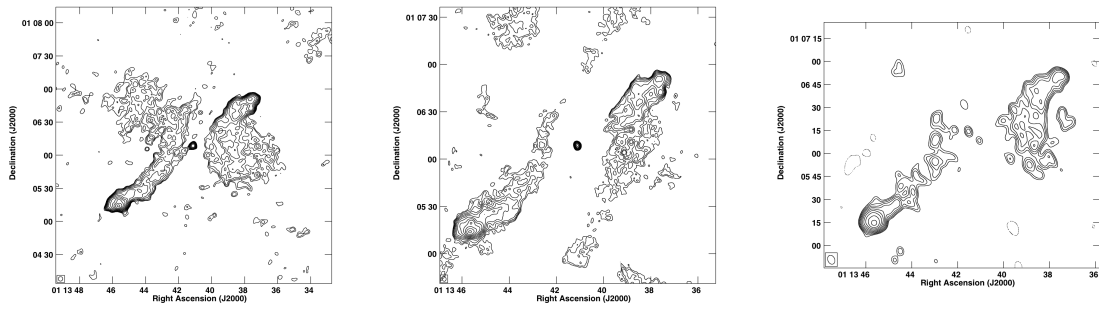
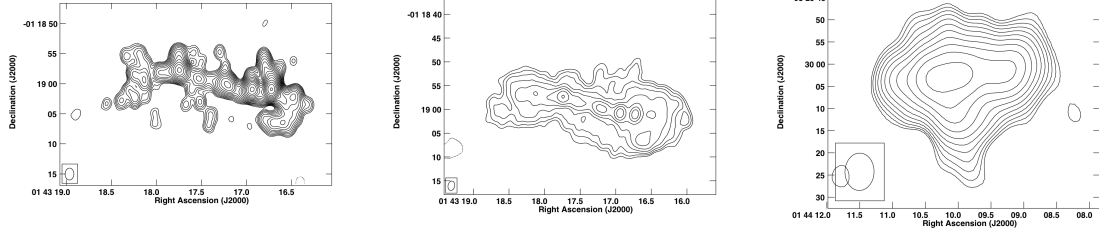
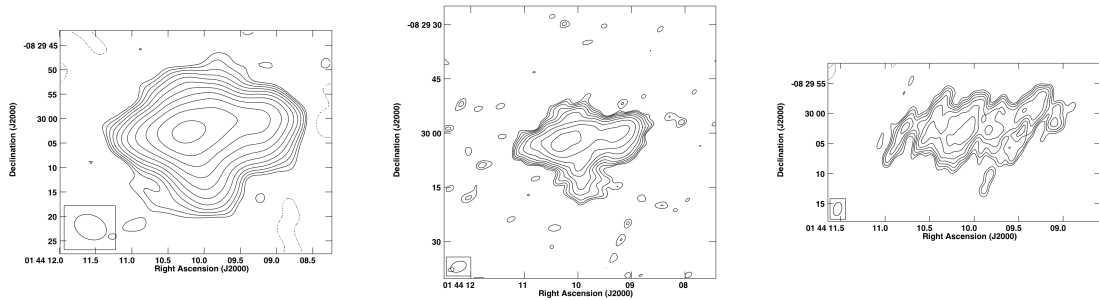


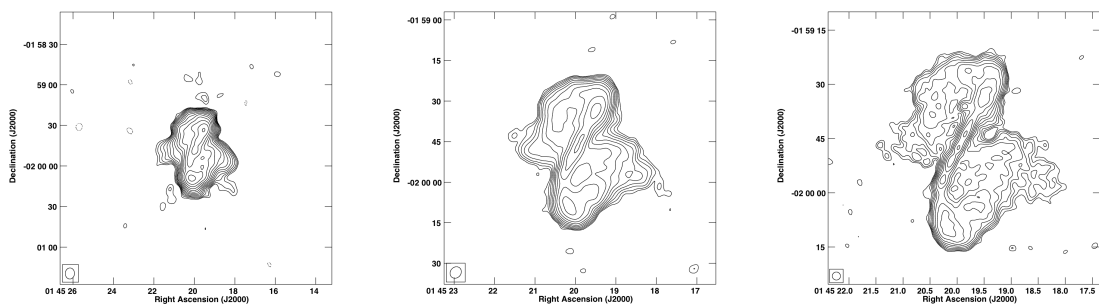
Fig. 3.—: VLA images of a sample of 100 low axial ratio radio sources (3/27).



(a) J0143–0119, B-array C-band.(b) J0143–0119, A-array L-band.(c) J0144–0830, C-array S-band.

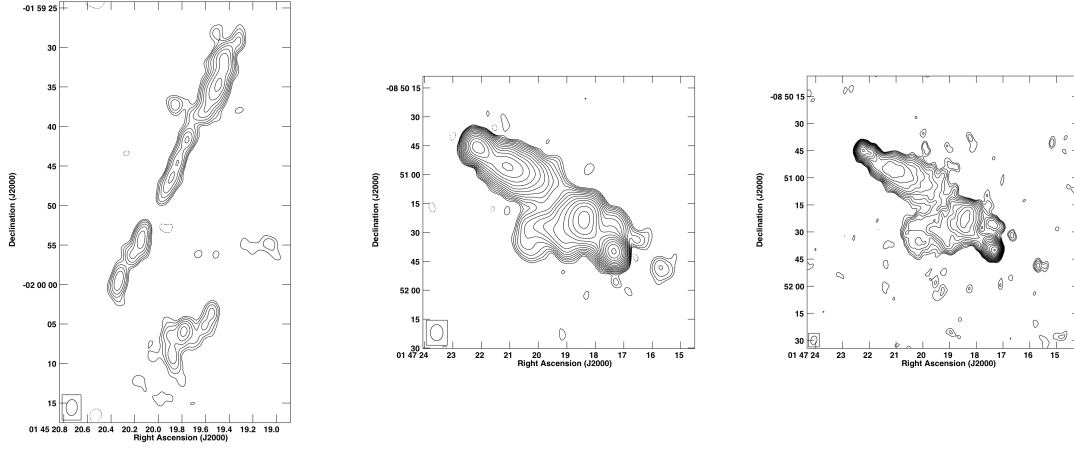


(d) J0144–0830, B-array L-band.(e) J0144–0830, B-array S-band.(f) J0144–0830, A-array L-band.

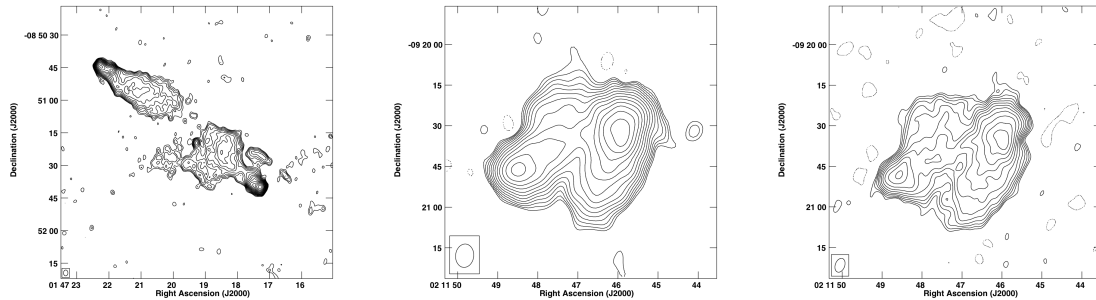


(g) J0145–0159, C-array S-band.(h) J0145–0159, B-array L-band. (i) J0145–0159, B-array S-band.

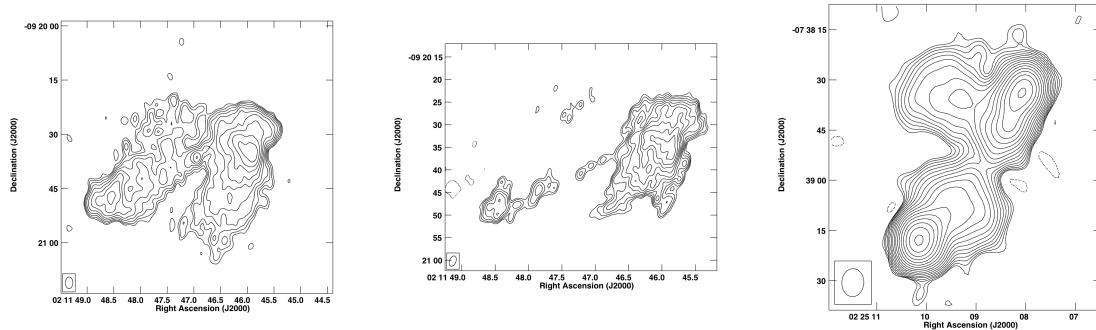
Fig. 4.—: VLA images of a sample of 100 low axial ratio radio sources (4/27).



(a) J0145–0159, A-array L-band.(b) J0147–0851, C-array S-band.(c) J0147–0851, B-array L-band.

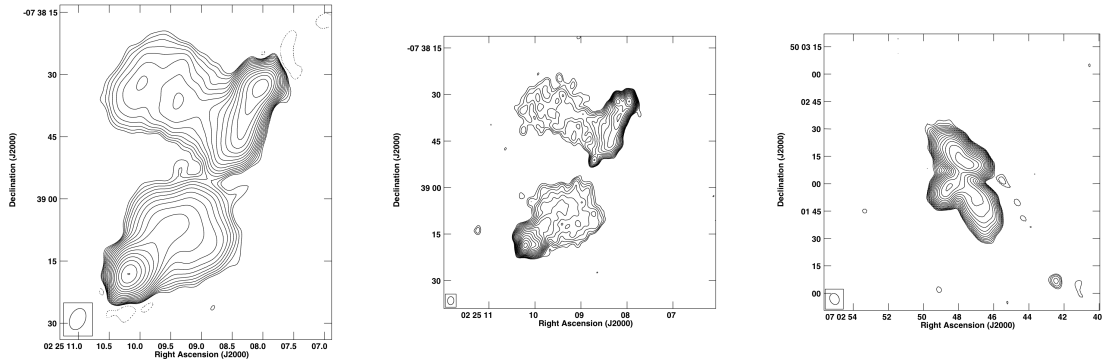


(d) J0147–0851, B-array S-band.(e) J0211–0920, C-array S-band.(f) J0211–0920, B-array L-band.

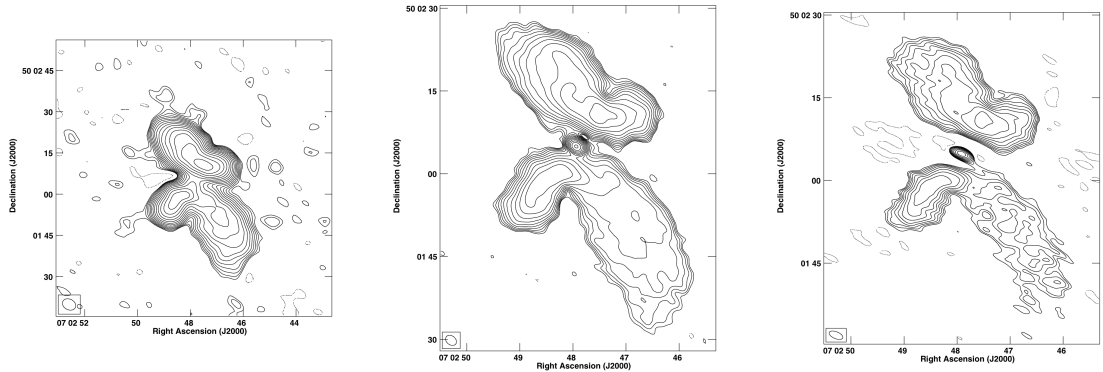


(g) J0211–0920, B-array S-band.(h) J0211–0920, A-array L-band.(i) J0225–0738, C-array S-band.

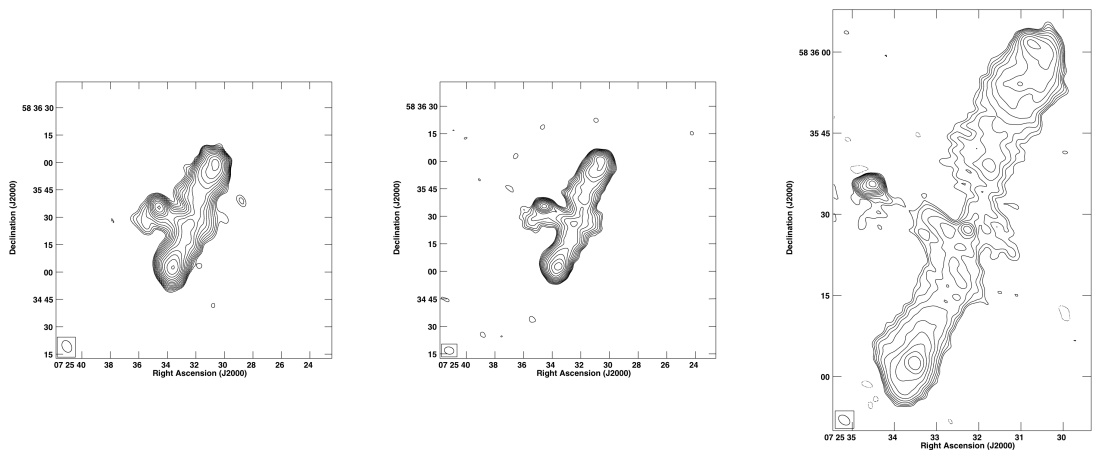
Fig. 5.—: VLA images of a sample of 100 low axial ratio radio sources (5/27).



(a) J0225–0738, B-array L-band.(b) J0225–0738, B-array S-band.(c) J0702+5002, C-array S-band.

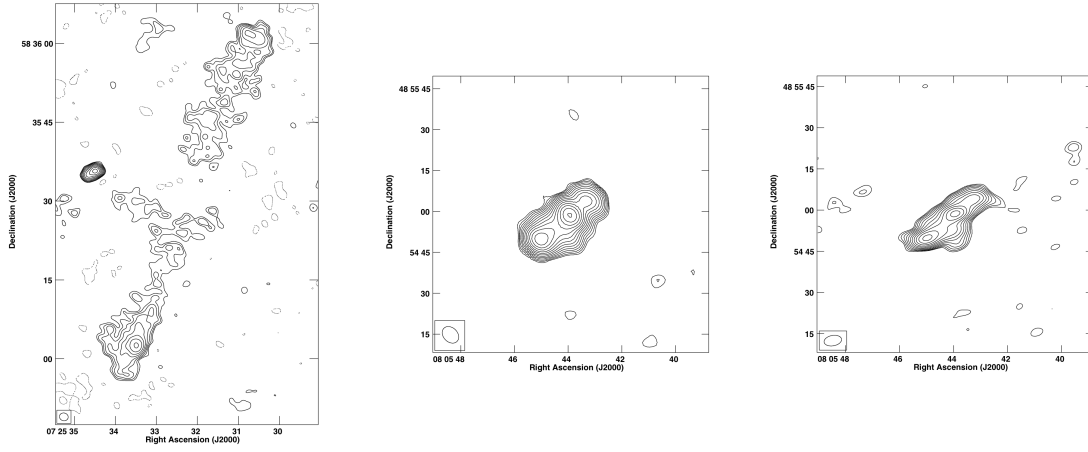


(d) J0702+5002, B-array L-band.(e) J0702+5002, B-array S-band.(f) J0702+5002, A-array L-band.

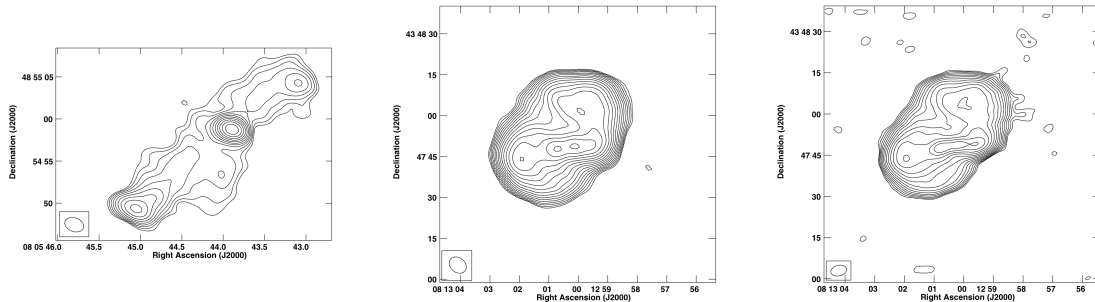


(g) J0725+5835, C-array S-band.(h) J0725+5835, B-array L-band.(i) J0725+5835, B-array S-band.

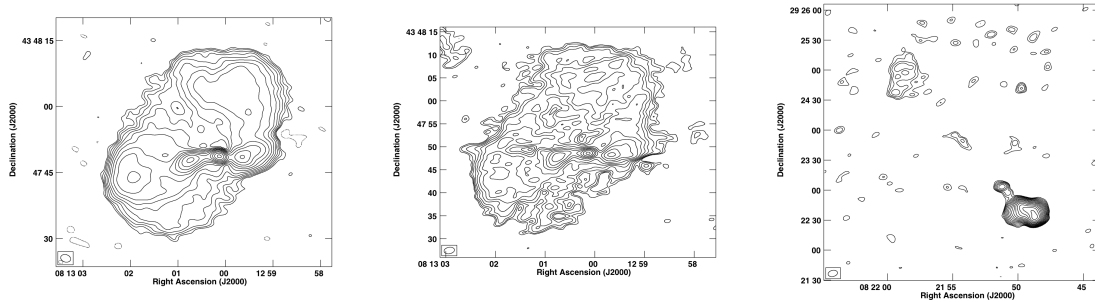
Fig. 6.—: VLA images of a sample of 100 low axial ratio radio sources (6/27).



(a) J0725+5835, A-array L-band.(b) J0805+4854, C-array S-band.(c) J0805+4854, B-array L-band.

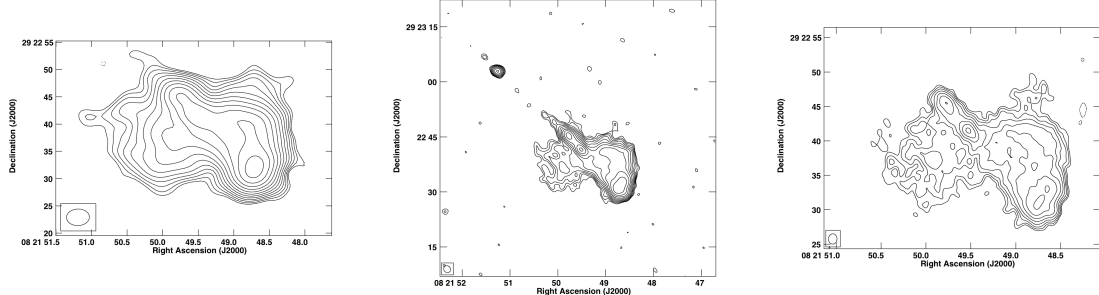


(d) J0805+4854, B-array S-band.(e) J0813+4347, C-array S-band.(f) J0813+4347, B-array L-band.

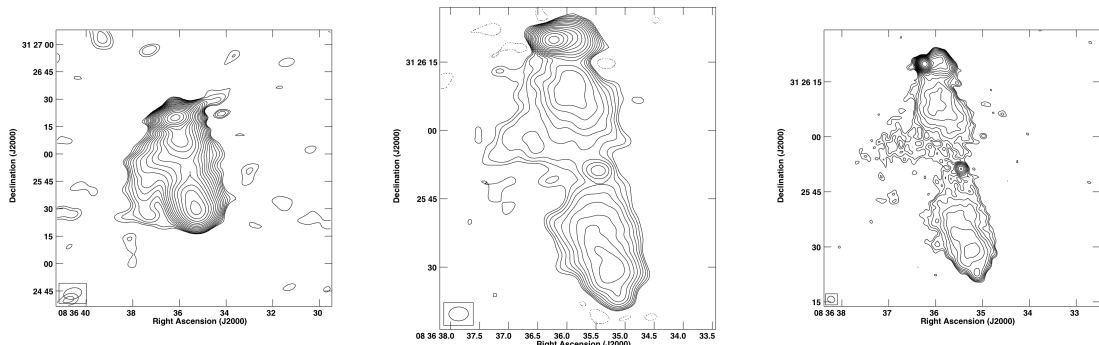


(g) J0813+4347, B-array S-band.(h) J0813+4347, A-array L-band. (i) J0821+2922, C-array S-band.

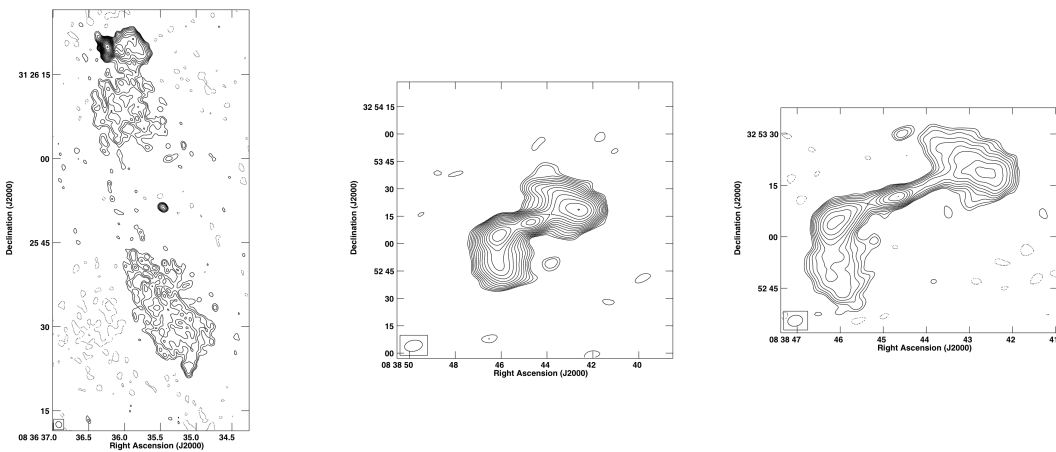
Fig. 7.—: VLA images of a sample of 100 low axial ratio radio sources (7/27).



(a) J0821+2922, B-array L-band.(b) J0821+2922, B-array S-band.(c) J0821+2922, A-array L-band.

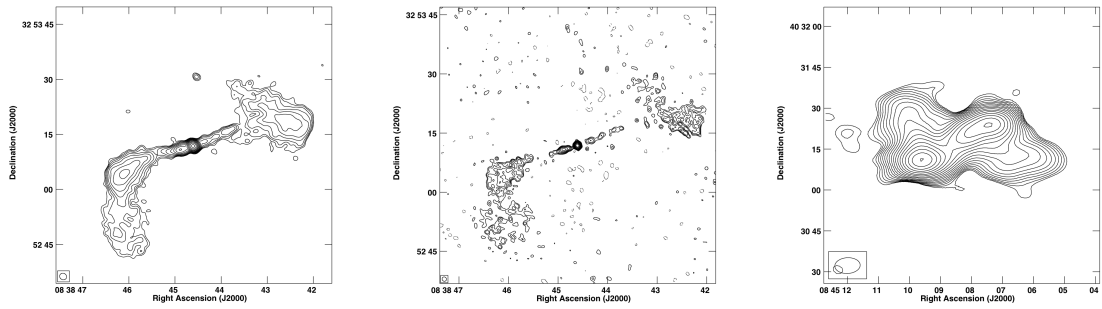


(d) J0836+3125, C-array S-band.(e) J0836+3125, B-array L-band.(f) J0836+3125, B-array S-band.

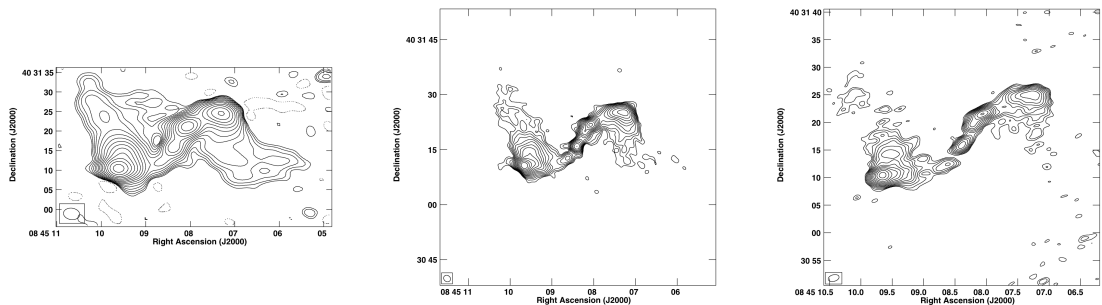


(g) J0836+3125, A-array L-band.(h) J0838+3253, C-array S-band.(i) J0838+3253, B-array L-band.

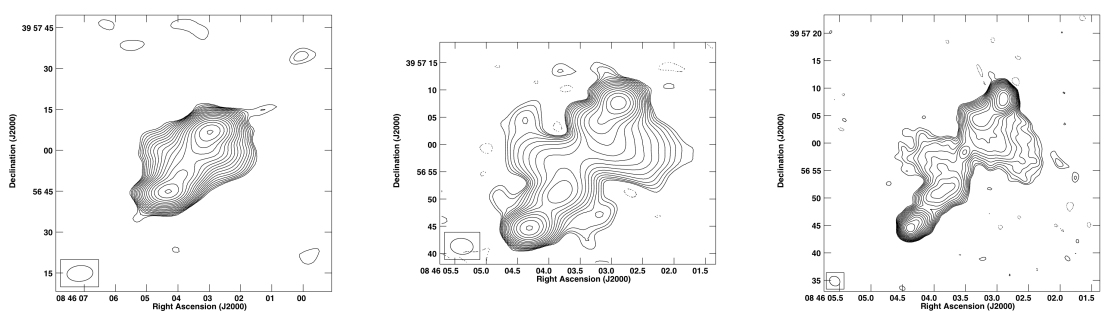
Fig. 8.—: VLA images of a sample of 100 low axial ratio radio sources (8/27).



(a) J0838+3253, B-array S-band.(b) J0838+3253, A-array L-band.(c) J0845+4031, C-array S-band.

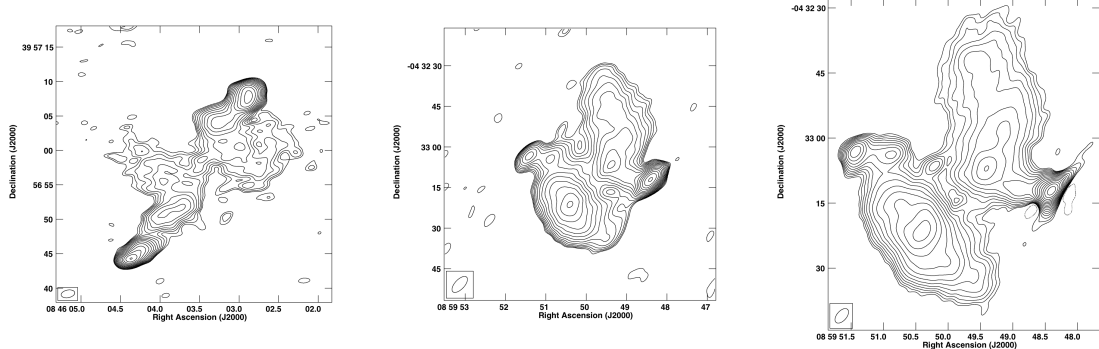


(d) J0845+4031, B-array L-band.(e) J0845+4031, B-array S-band.(f) J0845+4031, A-array L-band.

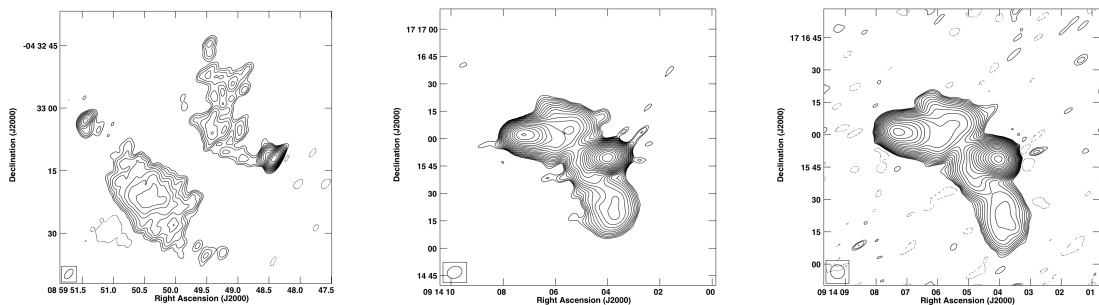


(g) J0846+3956, C-array S-band.(h) J0846+3956, B-array L-band. (i) J0846+3956, B-array S-band.

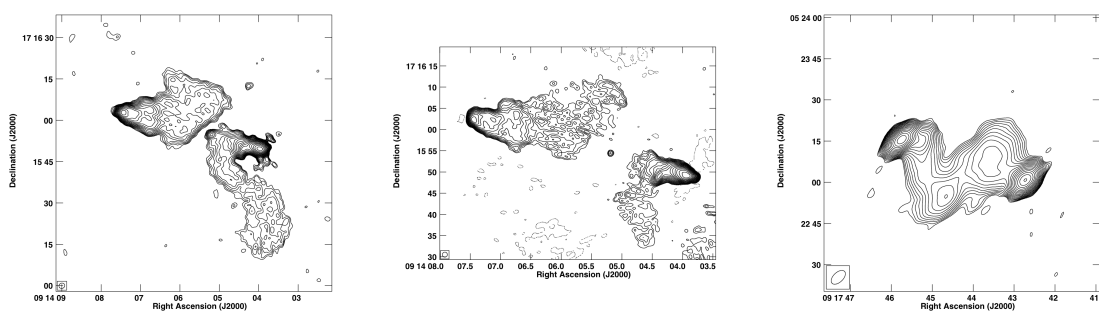
Fig. 9.—: VLA images of a sample of 100 low axial ratio radio sources (9/27).



(a) J0846+3956, A-array L-band.(b) J0859–0433, B-array L-band.(c) J0859–0433, B-array S-band.

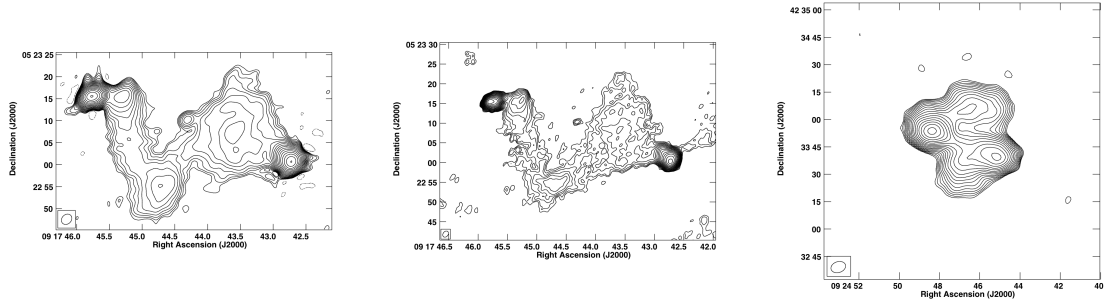


(d) J0859–0433, A-array L-band.(e) J0914+1715, C-array S-band.(f) J0914+1715, B-array L-band.

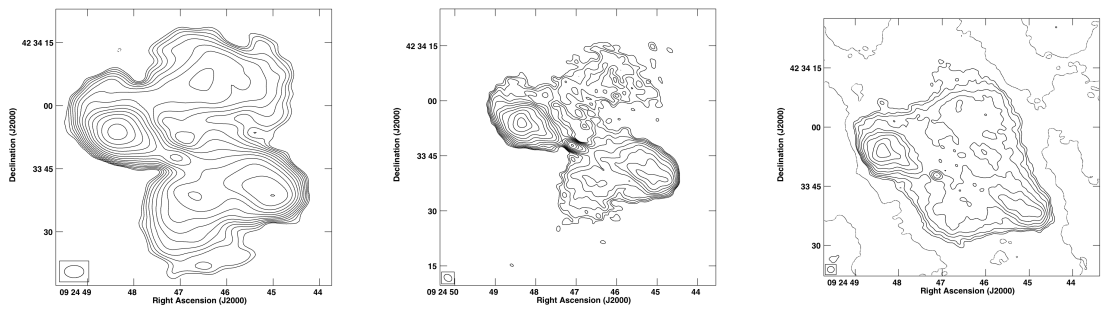


(g) J0914+1715, B-array S-band.(h) J0914+1715, A-array L-band.(i) J0917+0523, B-array L-band.

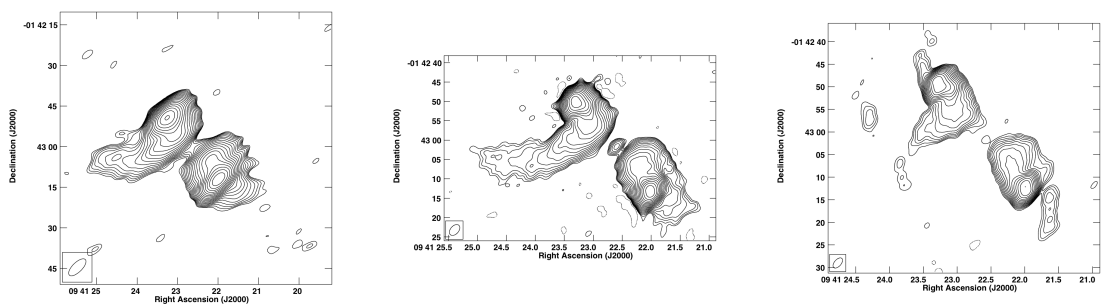
Fig. 10.—: VLA images of a sample of 100 low axial ratio radio sources (10/27).



(a) J0917+0523, B-array S-band.(b) J0917+0523, A-array L-band.(c) J0924+4233, C-array S-band.

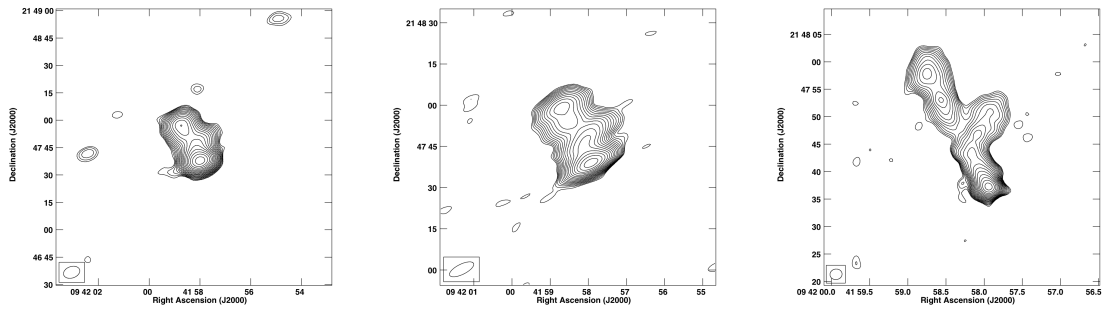


(d) J0924+4233, B-array L-band.(e) J0924+4233, B-array S-band.(f) J0924+4233, A-array L-band.

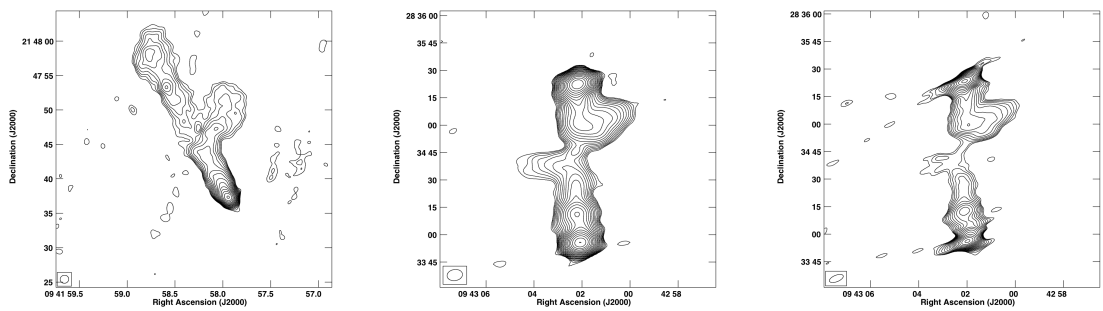


(g) J0941-0143, B-array L-band.(h) J0941-0143, B-array S-band.(i) J0941-0143, A-array L-band.

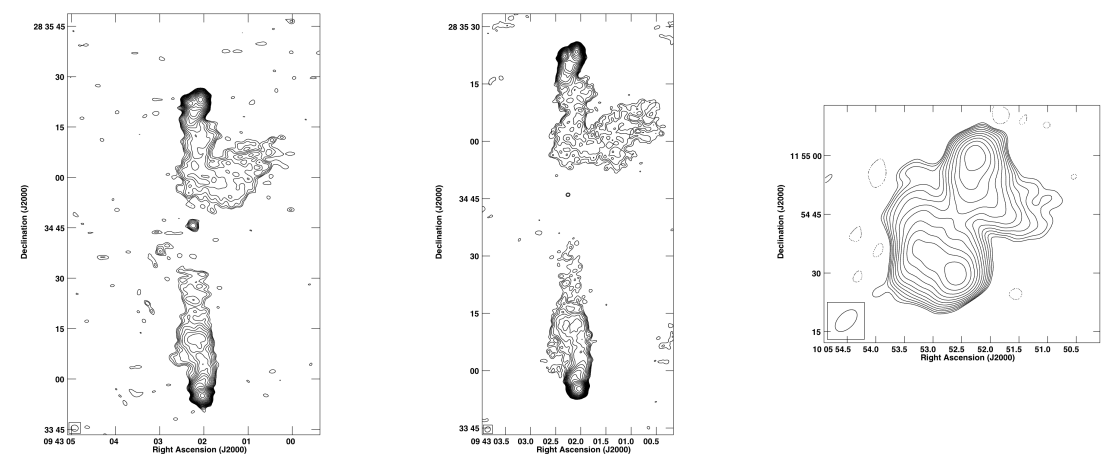
Fig. 11.—: VLA images of a sample of 100 low axial ratio radio sources (11/27).



(a) J0941+2147, C-array S-band.(b) J0941+2147, B-array L-band.(c) J0941+2147, B-array S-band.

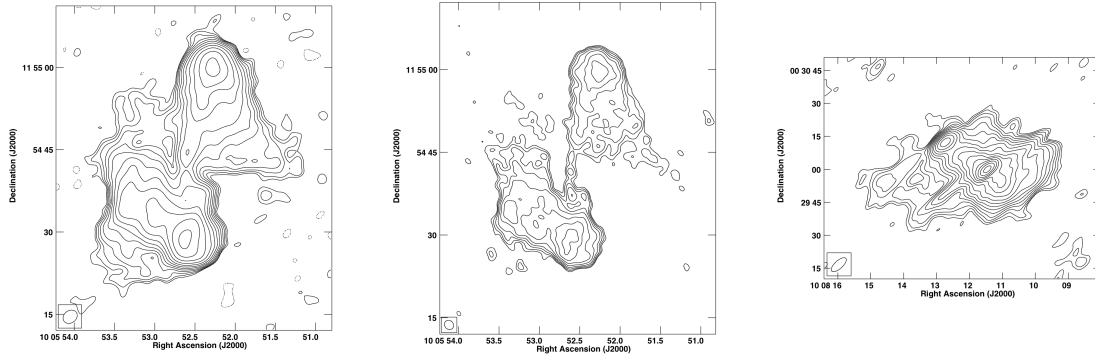


(d) J0941+2147, A-array L-band.(e) J0943+2834, C-array S-band.(f) J0943+2834, B-array L-band.

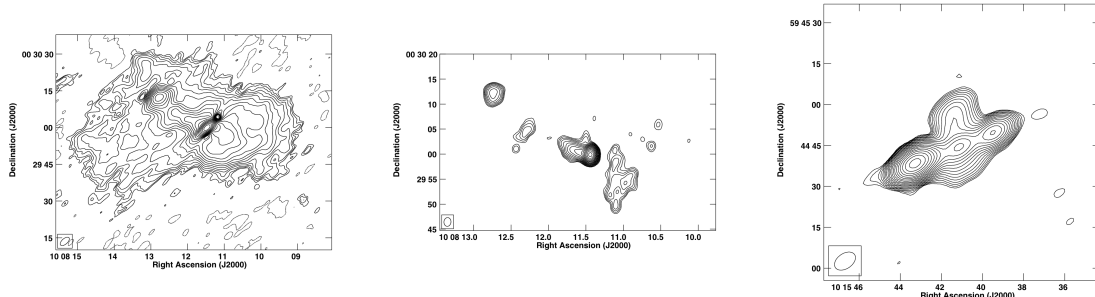


(g) J0943+2834, B-array S-band.(h) J0943+2834, A-array L-band.(i) J1005+1154, B-array L-band.

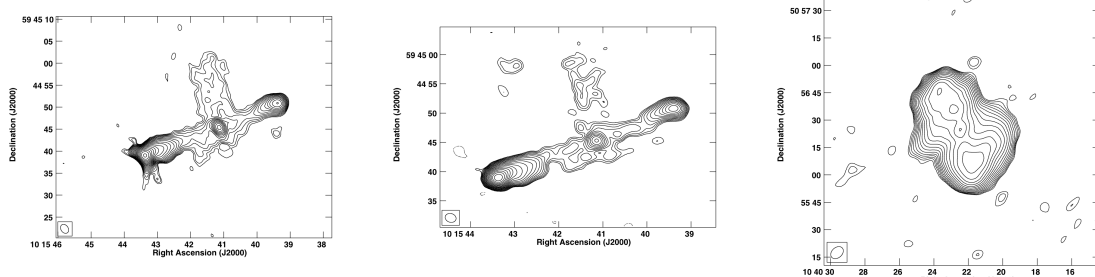
Fig. 12.—: VLA images of a sample of 100 low axial ratio radio sources (12/27).



(a) J1005+1154, B-array S-band.(b) J1005+1154, A-array L-band.(c) J1008+0030, B-array L-band.

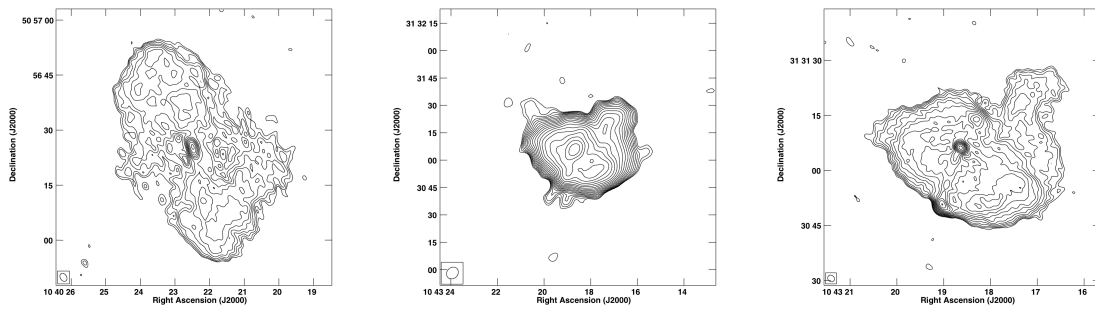


(d) J1008+0030, B-array S-band.(e) J1008+0030, A-array L-band.(f) J1015+5944, C-array S-band.

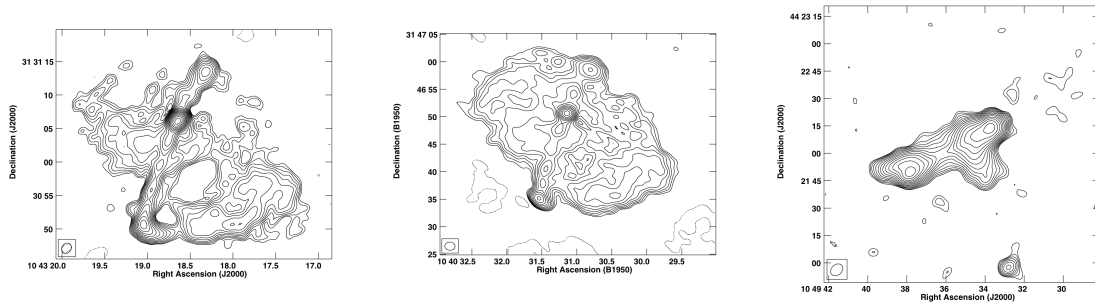


(g) J1015+5944, B-array S-band.(h) J1015+5944, A-array L-band.(i) J1040+5056, C-array S-band.

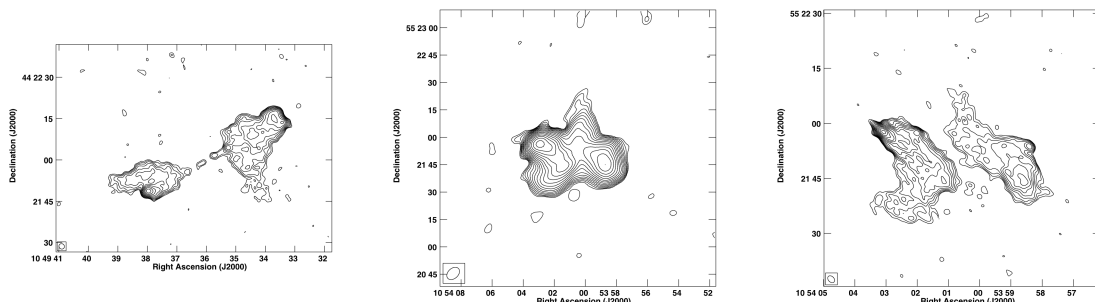
Fig. 13.—: VLA images of a sample of 100 low axial ratio radio sources (13/27).



(a) J1040+5056, B-array S-band.(b) J1043+3131, C-array S-band.(c) J1043+3131, B-array S-band.

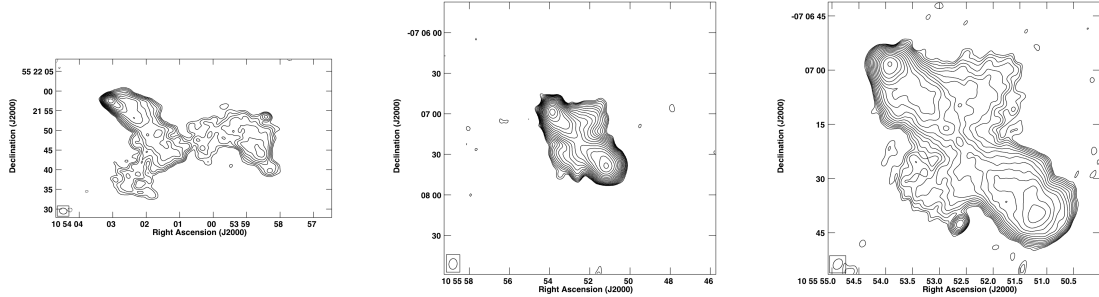


(d) J1043+3131, B-array C-band.(e) J1043+3131, A-array L-band.(f) J1049+4422, C-array S-band.

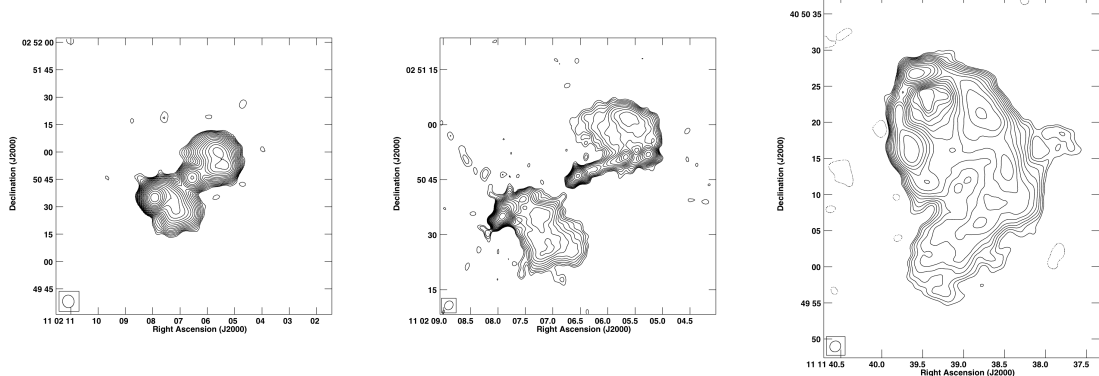


(g) J1049+4422, B-array S-band.(h) J1054+5521, C-array S-band.(i) J1054+5521, B-array S-band.

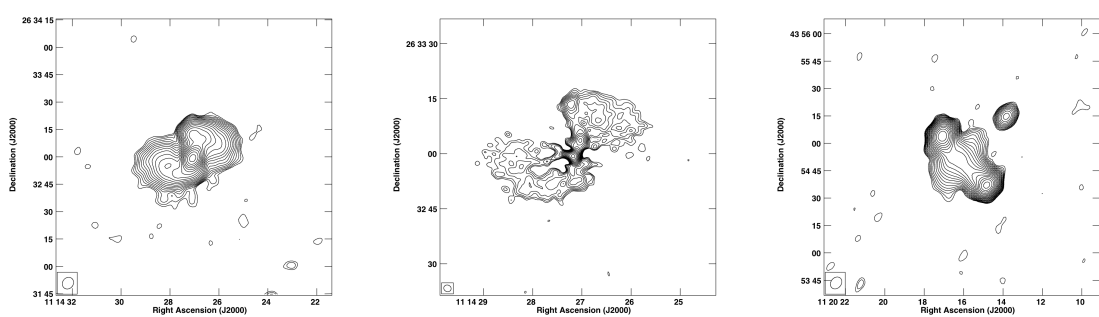
Fig. 14.—: VLA images of a sample of 100 low axial ratio radio sources (14/27).



(a) J1054+5521, A-array L-band.(b) J1055-0707, C-array S-band.(c) J1055-0707, B-array S-band.

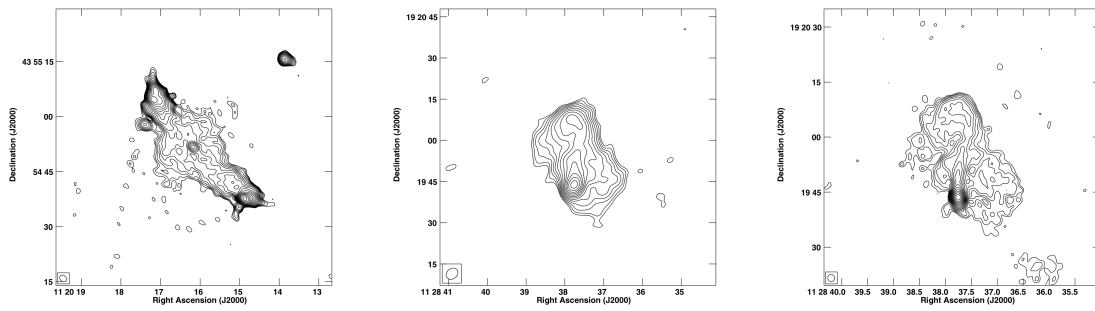


(d) J1102+0250, C-array S-band.(e) J1102+0250, B-array S-band.(f) J1111+4050, B-array C-band.

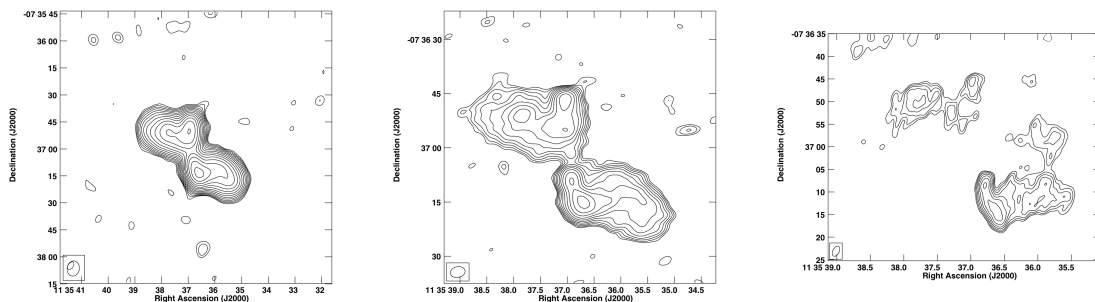


(g) J1114+2632, C-array S-band.(h) J1114+2632, B-array S-band.(i) J1120+4354, C-array S-band.

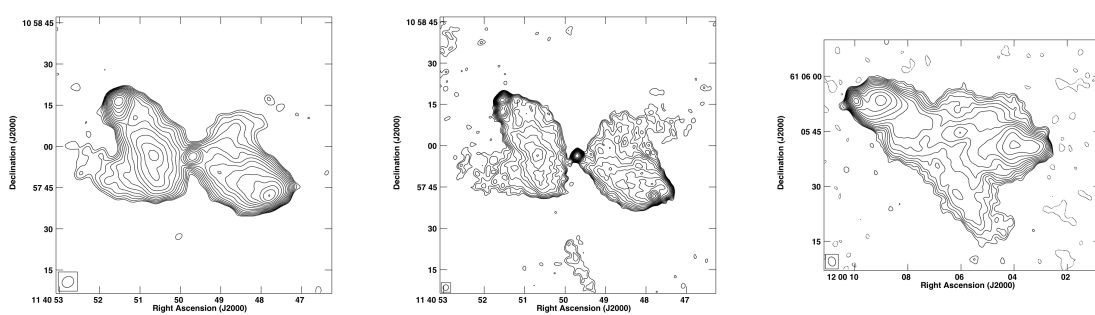
Fig. 15.—: VLA images of a sample of 100 low axial ratio radio sources (15/27).



(a) J1120+4354, B-array S-band.(b) J1128+1919, B-array L-band.(c) J1128+1919, B-array S-band.

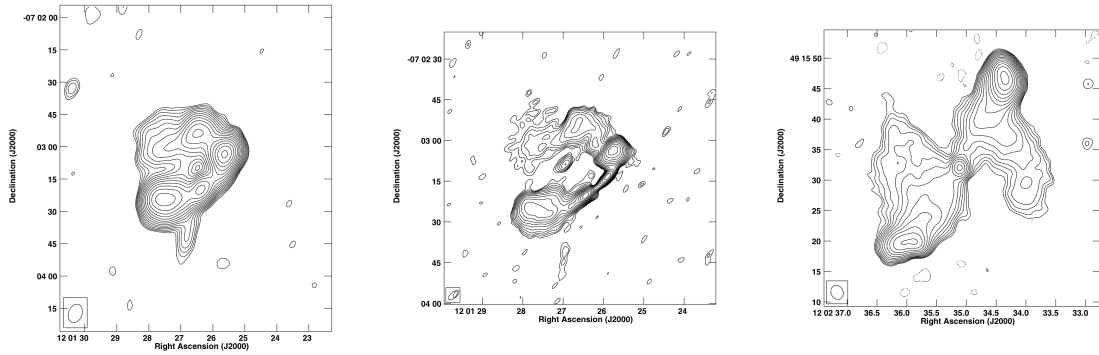


(d) J1135-0737, C-array S-band.(e) J1135-0737, B-array S-band.(f) J1135-0737, A-array L-band.

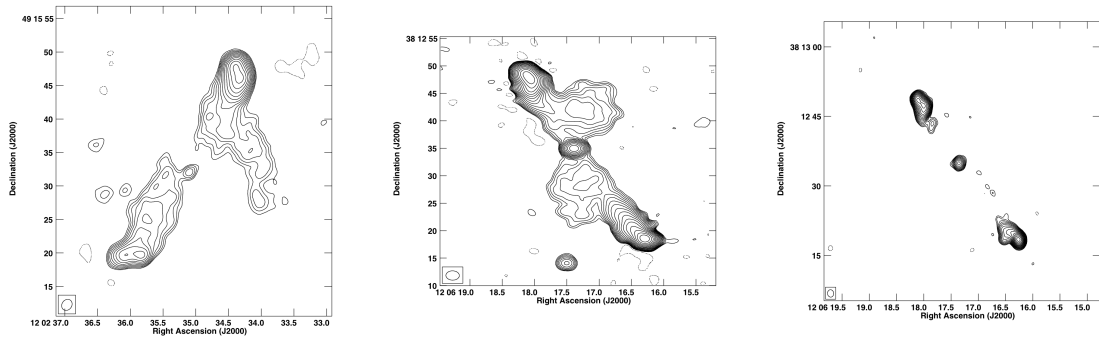


(g) J1140+1057, B-array L-band.(h) J1140+1057, B-array S-band.(i) J1200+6105, B-array S-band.

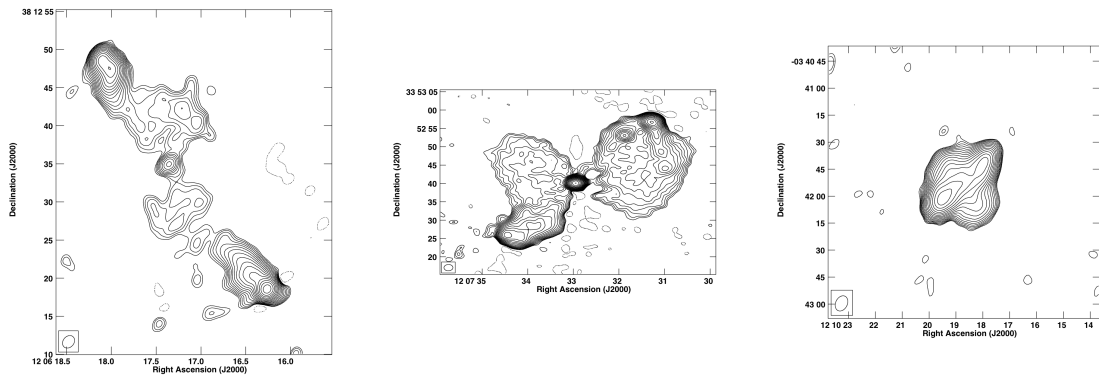
Fig. 16.—: VLA images of a sample of 100 low axial ratio radio sources (16/27).



(a) J1201–0703, C-array S-band.(b) J1201–0703, B-array S-band.(c) J1202+4915, B-array S-band.

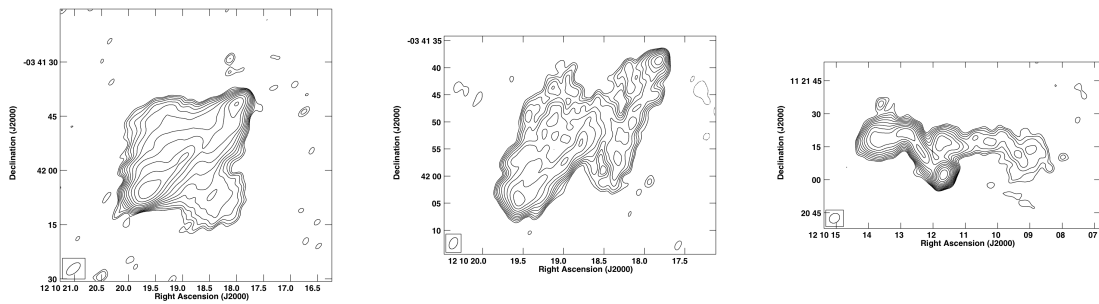


(d) J1202+4915, A-array L-band.(e) J1206+3812, B-array S-band.(f) J1206+3812, B-array C-band.

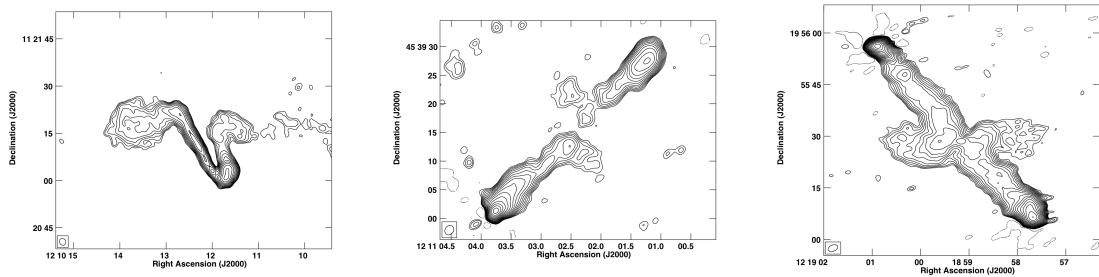


(g) J1206+3812, A-array L-band.(h) J1207+3352, B-array S-band.(i) J1210–0341, C-array S-band.

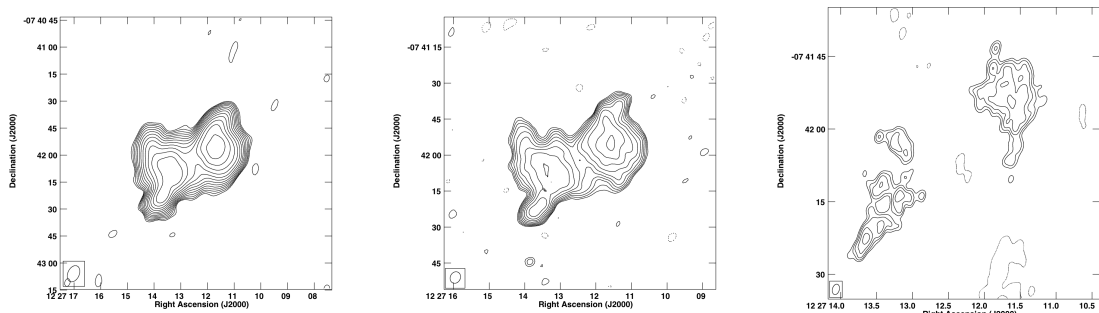
Fig. 17.—: VLA images of a sample of 100 low axial ratio radio sources (17/27).



(a) J1210–0341, B-array S-band.(b) J1210–0341, A-array L-band.(c) J1210+1121, B-array L-band.

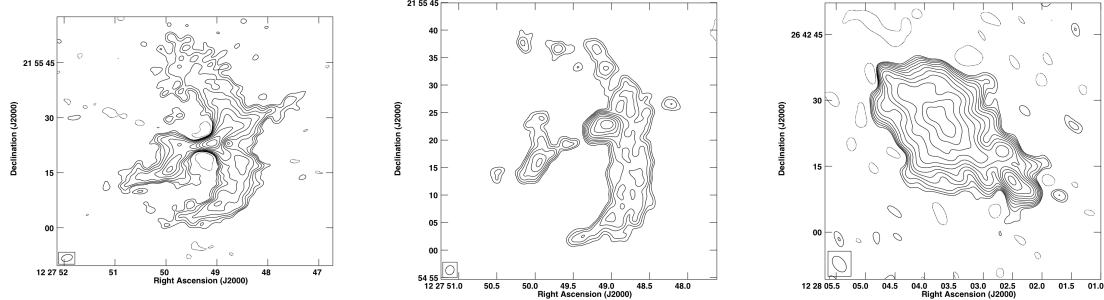


(d) J1210+1121, B-array S-band.(e) J1211+4539, A-array L-band.(f) J1218+1955, B-array S-band.

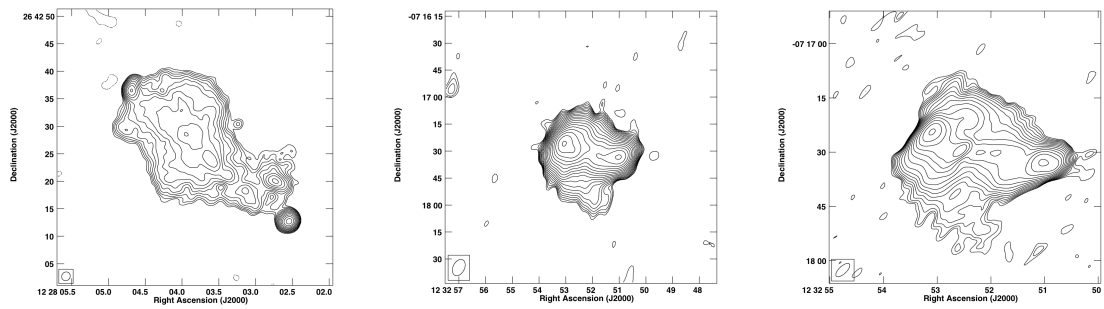


(g) J1227–0742, C-array S-band.(h) J1227–0742, B-array S-band.(i) J1227–0742, A-array L-band.

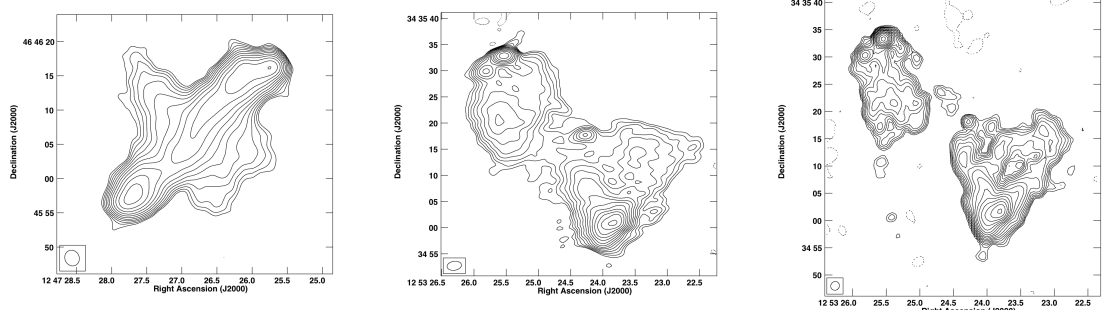
Fig. 18.—: VLA images of a sample of 100 low axial ratio radio sources (18/27).



(a) J1227+2155, B-array S-band.(b) J1227+2155, A-array L-band.(c) J1228+2642, B-array S-band.

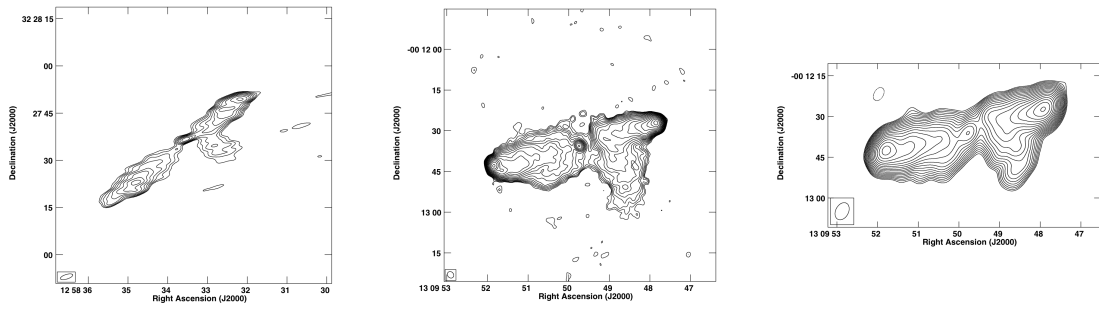


(d) J1228+2642, A-array L-band.(e) J1232-0717, C-array S-band.(f) J1232-0717, B-array S-band.

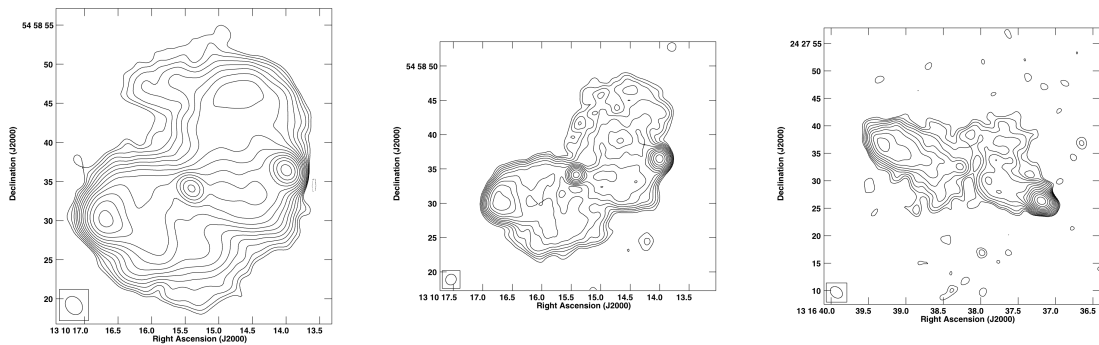


(g) J1247+4646, B-array S-band.(h) J1253+3435, B-array S-band.(i) J1253+3435, A-array L-band.

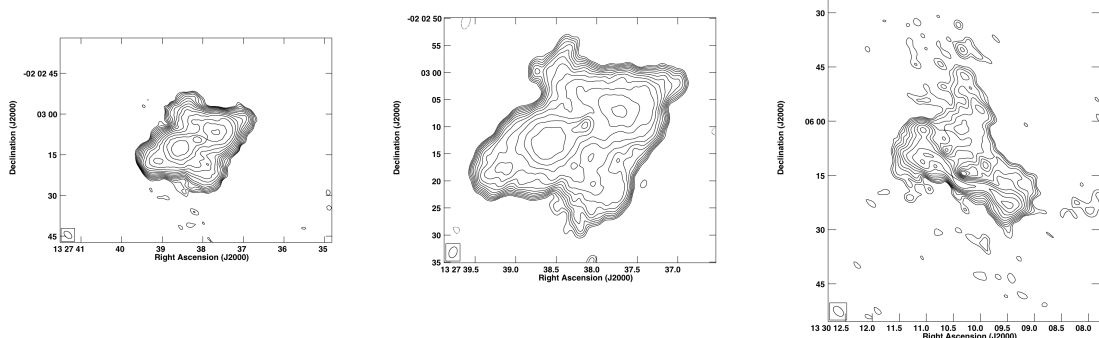
Fig. 19.—: VLA images of a sample of 100 low axial ratio radio sources (19/27).



(a) J1258+3227, B-array S-band.(b) J1309–0012, B-array S-band.(c) J1309–0012, B-array C-band.

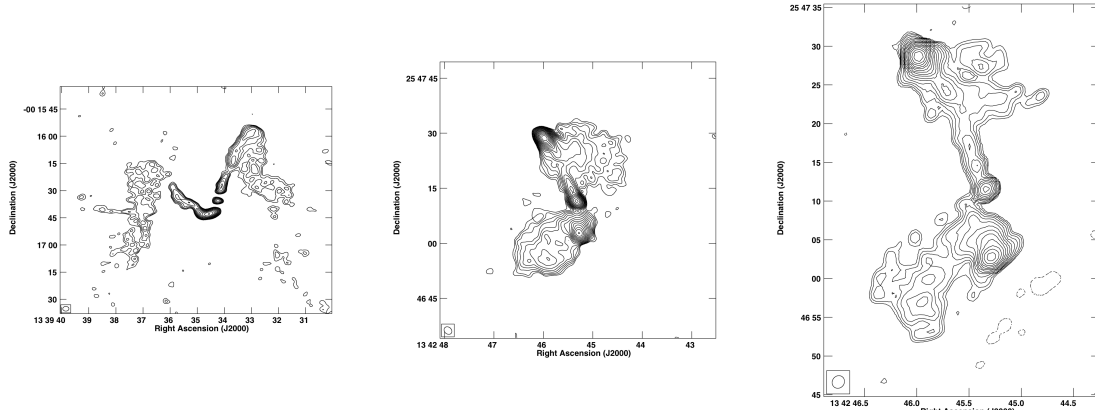


(d) J1310+5458, B-array S-band.(e) J1310+5458, A-array L-band.(f) J1316+2427, B-array S-band.

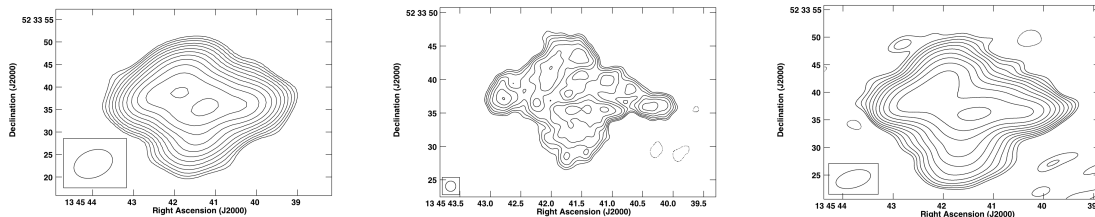


(g) J1327–0203, B-array S-band.(h) J1327–0203, A-array L-band.(i) J1330–0206, B-array S-band.

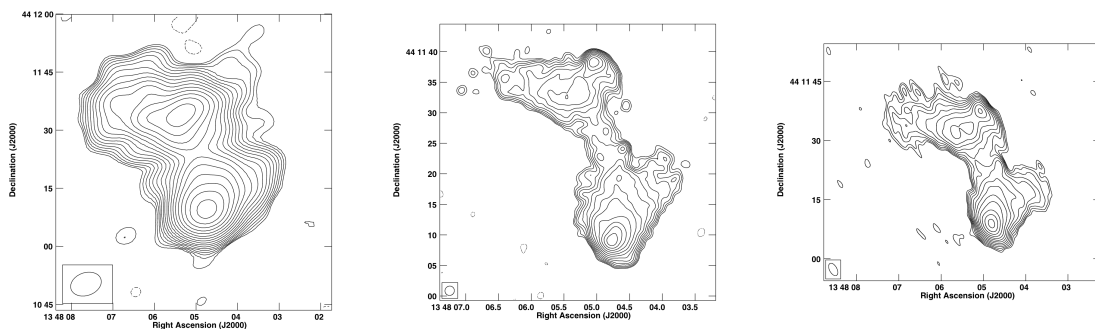
Fig. 20.—: VLA images of a sample of 100 low axial ratio radio sources (20/27).



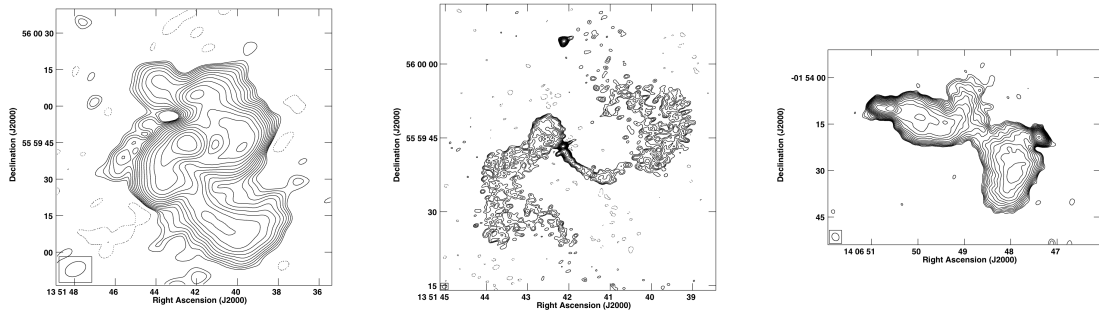
(a) J1339–0016, B-array S-band.(b) J1342+2547, B-array S-band.(c) J1342+2547, A-array L-band.



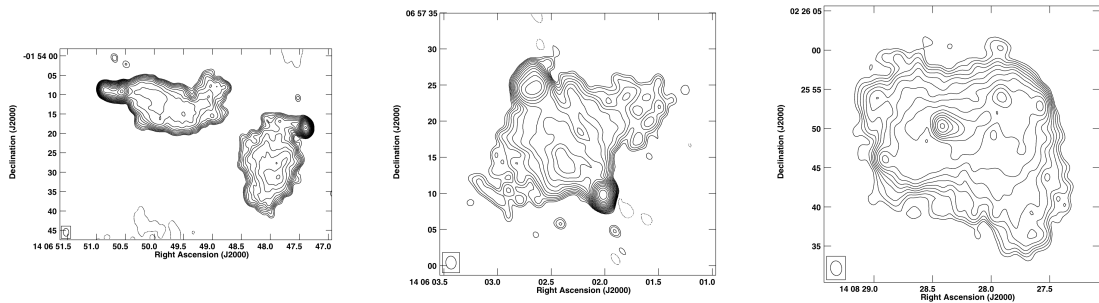
(d) J1345+5233, C-array S-band.(e) J1345+5233, A-array L-band.(f) J1345+5233, AB-array S-band.



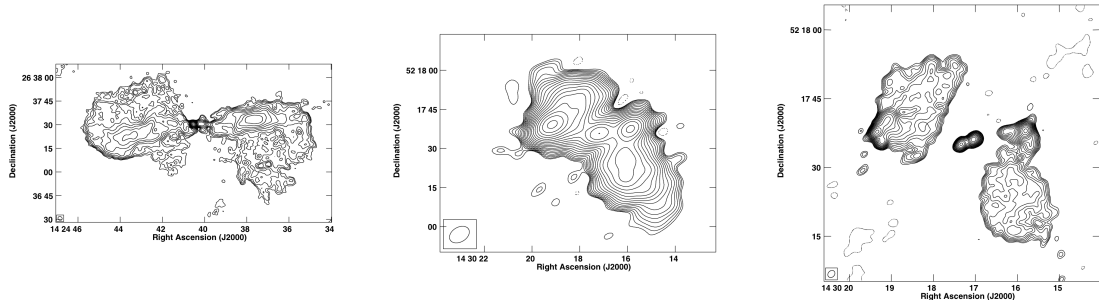
(g) J1348+4411, C-array S-band.(h) J1348+4411, A-array L-band.(i) J1348+4411, AB-array S-band.



(a) J1351+5559, C-array S-band.(b) J1351+5559, AB-array S-(c) J1406-0154, B-array S-band.

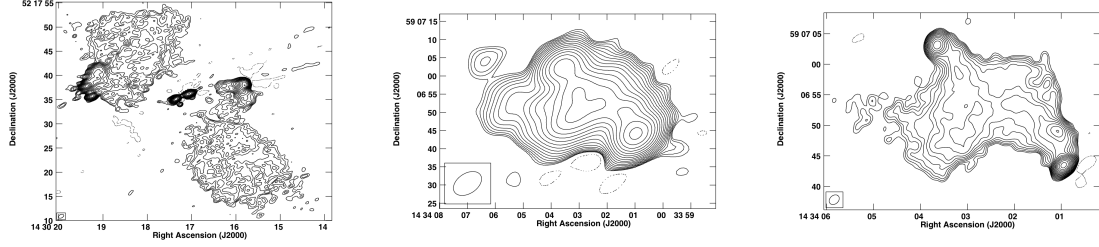


(d) J1406-0154, A-array L-band.(e) J1406+0657, A-array L-band.(f) J1408+0225, A-array L-band.

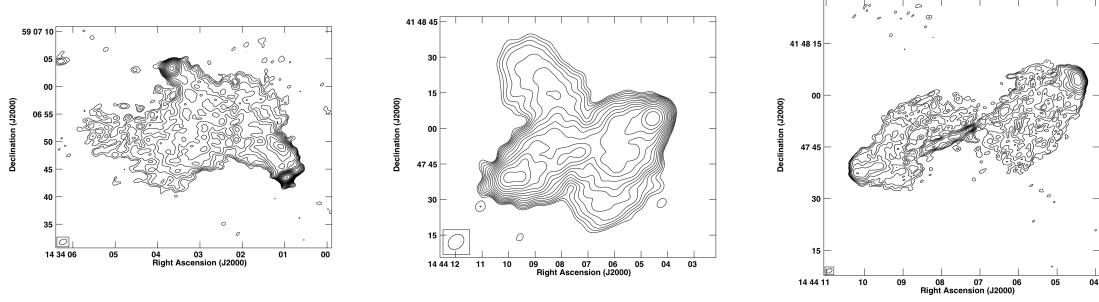


(g) J1424+2637, B-array S-band.(h) J1430+5217, C-array S-band.(i) J1430+5217, A-array L-band.

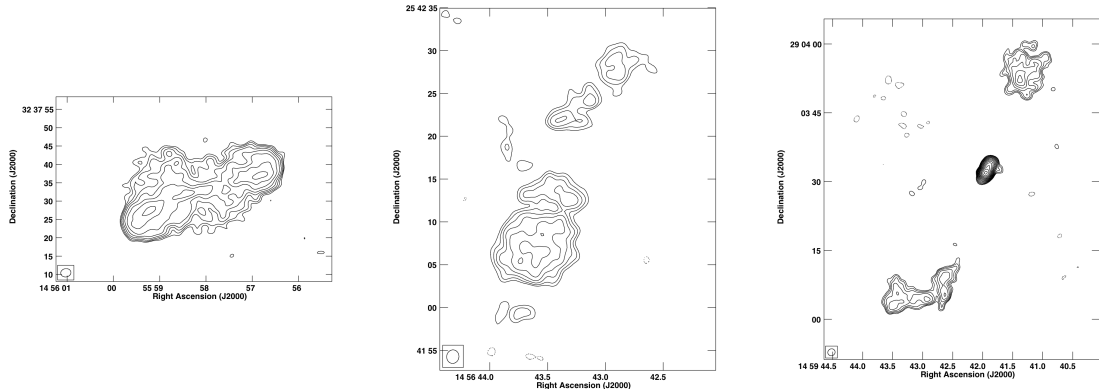
Fig. 22.—: VLA images of a sample of 100 low axial ratio radio sources (22/27).



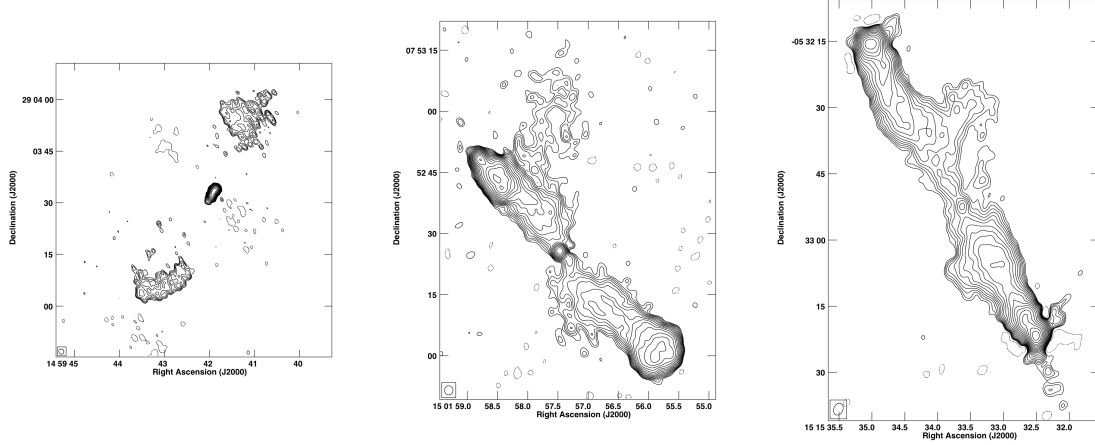
(a) J1430+5217, AB-array S-(b) J1434+5906, C-array S-band.(c) J1434+5906, A-array L-band.
band.



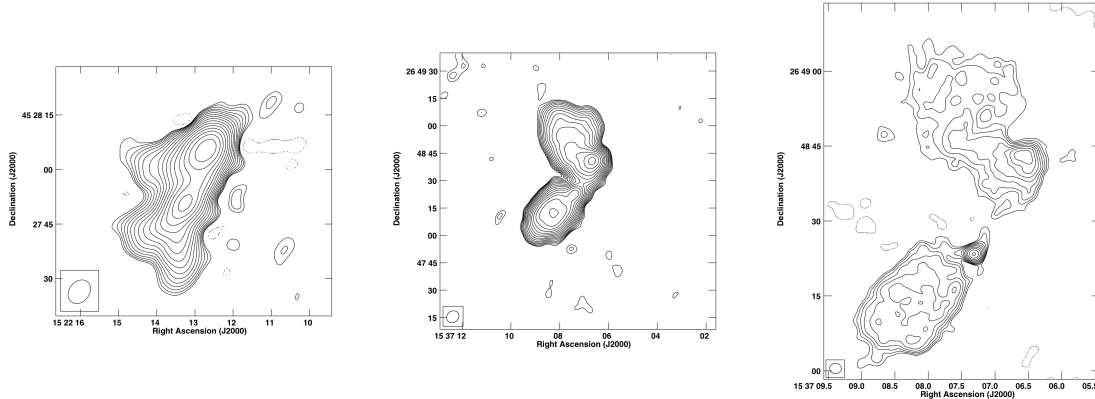
(d) J1434+5906, AB-array S-(e) J1444+4147, C-array S-band.(f) J1444+4147, AB-array S-
band.



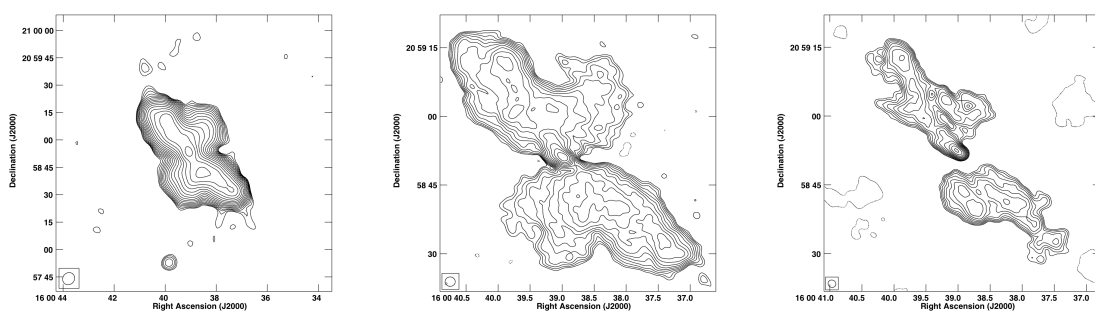
(g) J1455+3237, B-array S-band.(h) J1456+2542, A-array L-band.(i) J1459+2903, B-array C-band.



(a) J1459+2903, A-array L-band.(b) J1501+0752, B-array S-band.(c) J1515–0532, B-array S-band.

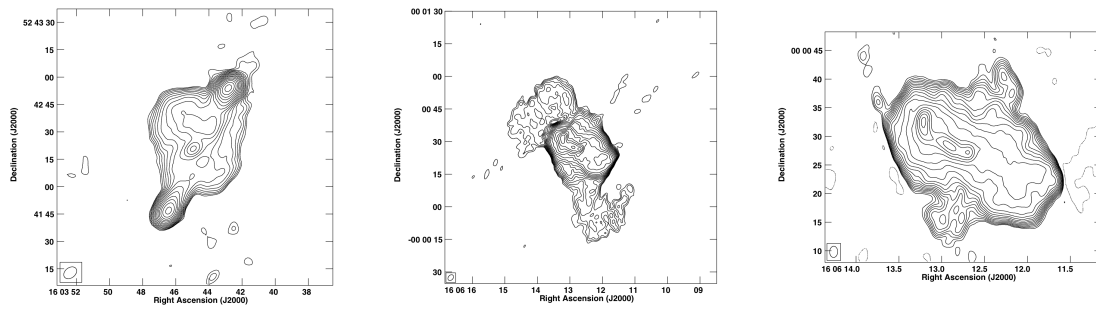


(d) J1522+4527, C-array S-band.(e) J1537+2648, C-array S-band.(f) J1537+2648, B-array S-band.

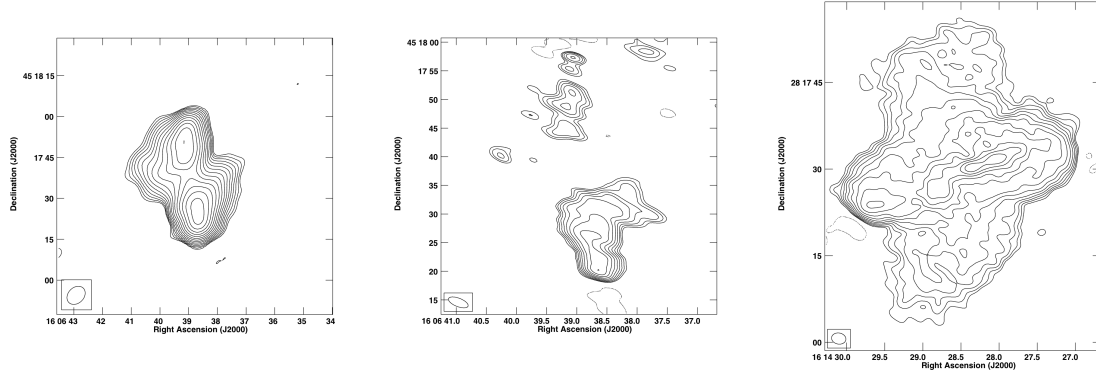


(g) J1600+2058, C-array S-band.(h) J1600+2058, B-array S-band.(i) J1600+2058, A-array L-band.

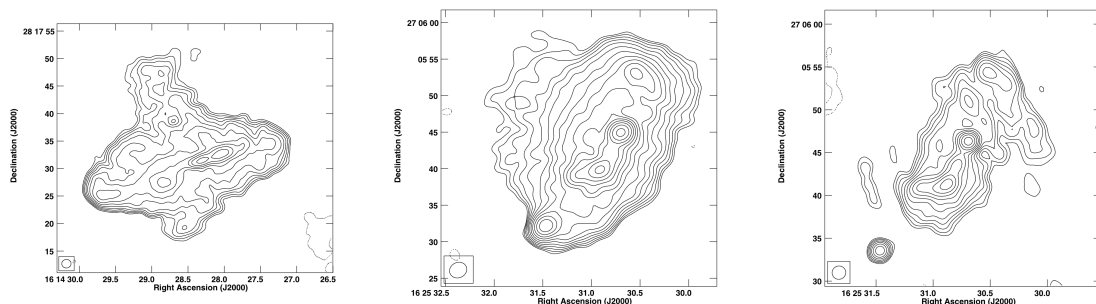
Fig. 24.—: VLA images of a sample of 100 low axial ratio radio sources (24/27).



(a) J1603+5242, C-array S-band.(b) J1606+0000, B-array S-band.(c) J1606+0000, A-array L-band.

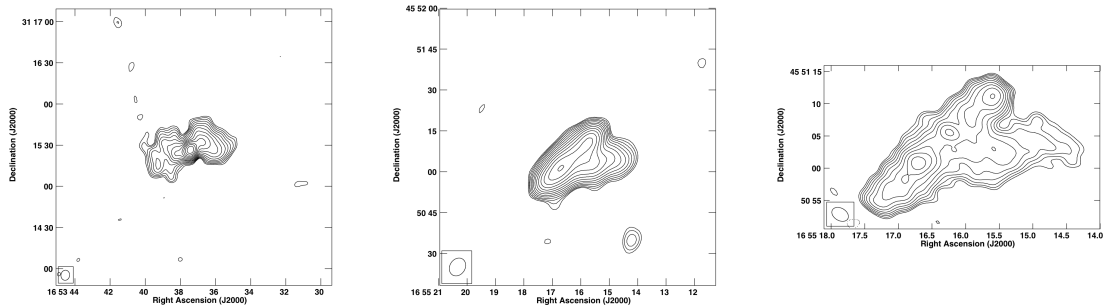


(d) J1606+4517, C-array S-band.(e) J1606+4517, A-array L-band.(f) J1614+2817, B-array S-band.

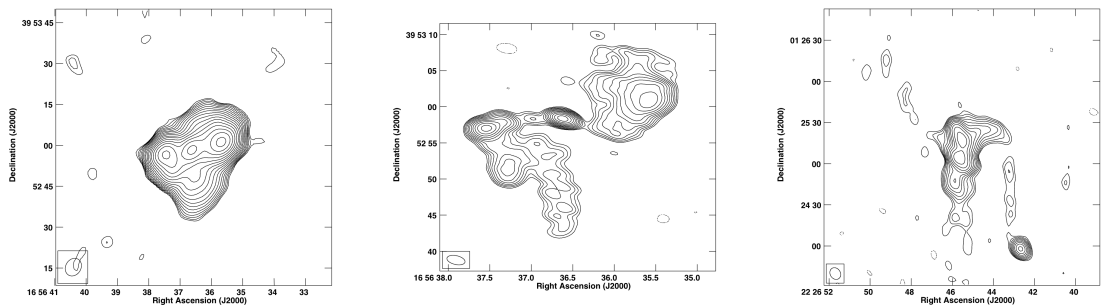


(g) J1614+2817, A-array L-band.(h) J1625+2705, B-array S-band.(i) J1625+2705, A-array L-band.

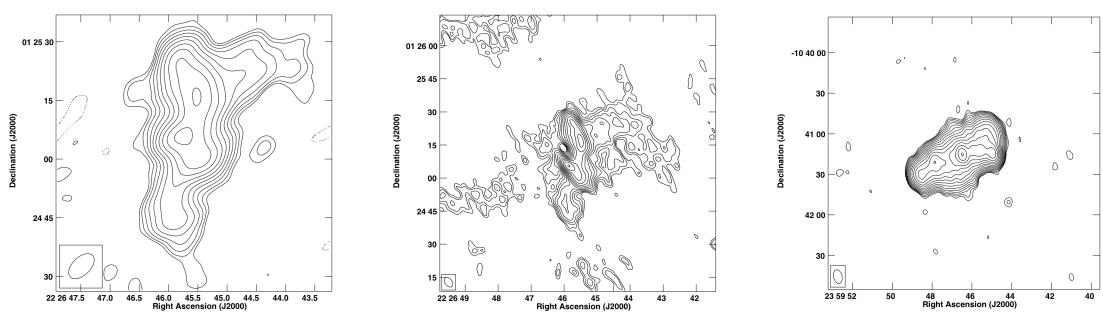
Fig. 25.—: VLA images of a sample of 100 low axial ratio radio sources (25/27).



(a) J1653+3115, C-array S-band.(b) J1655+4551, C-array S-band.(c) J1655+4551, B-array S-band.

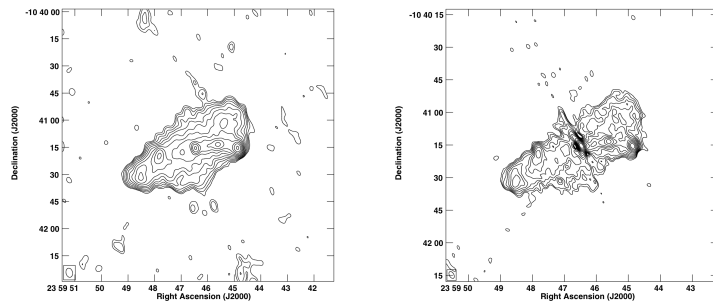


(d) J1656+3952, C-array S-band.(e) J1656+3952, A-array L-band.(f) J2226+0125, C-array S-band.



(g) J2226+0125, B-array L-band.(h) J2226+0125, B-array S-band.(i) J2359-1041, C-array S-band.

Fig. 26.—: VLA images of a sample of 100 low axial ratio radio sources (26/27).



(a) J2359–1041, B-array L-band.(b) J2359–1041, B-array S-band.

Fig. 27.—: VLA images of a sample of 100 low axial ratio radio sources (27/27).

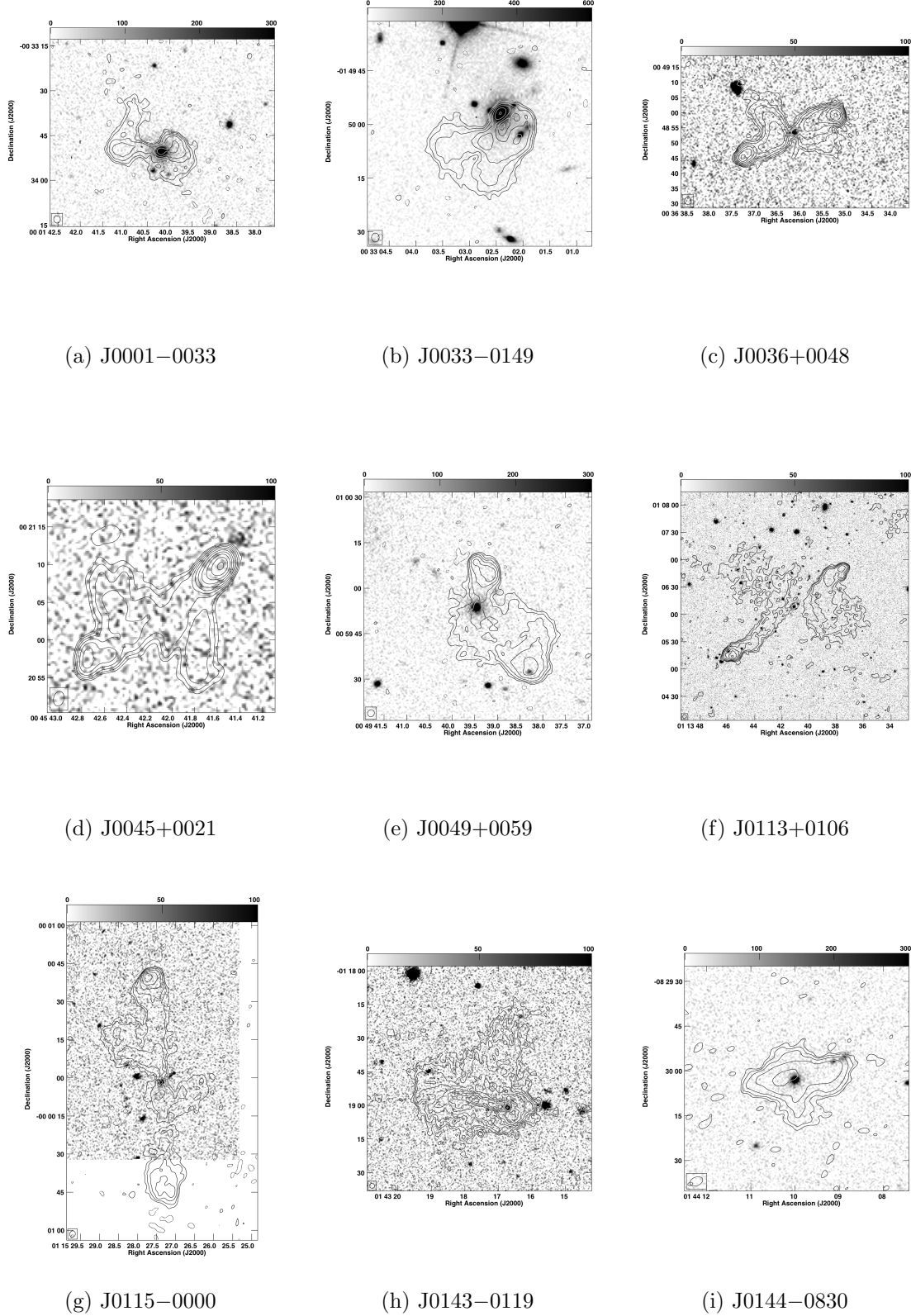


Fig. 28.— Optical overlays of a sample of 100 low axial ratio radio sources (1/11).

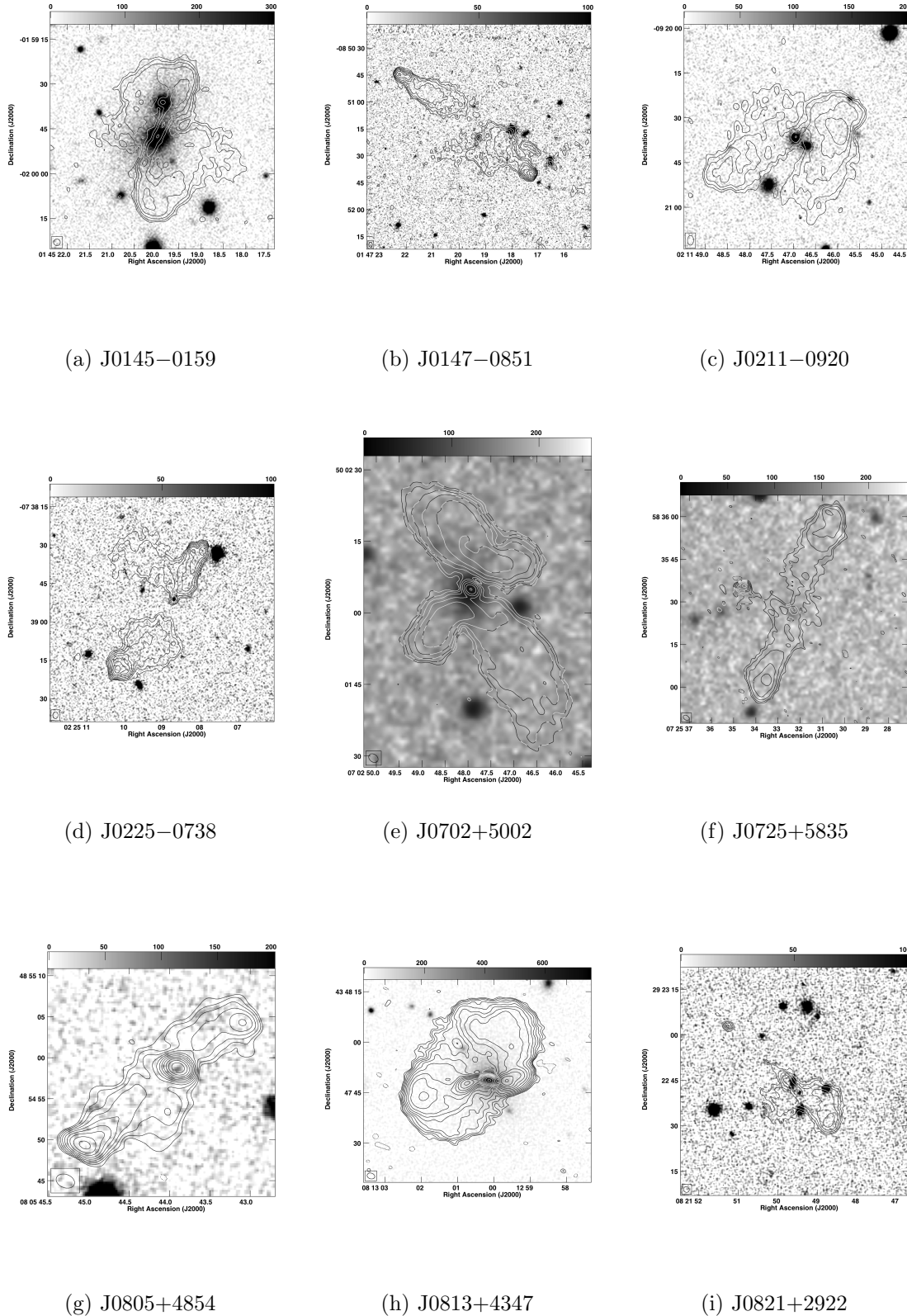


Fig. 29.— Optical overlays of a sample of 100 low axial ratio radio sources (2/11).

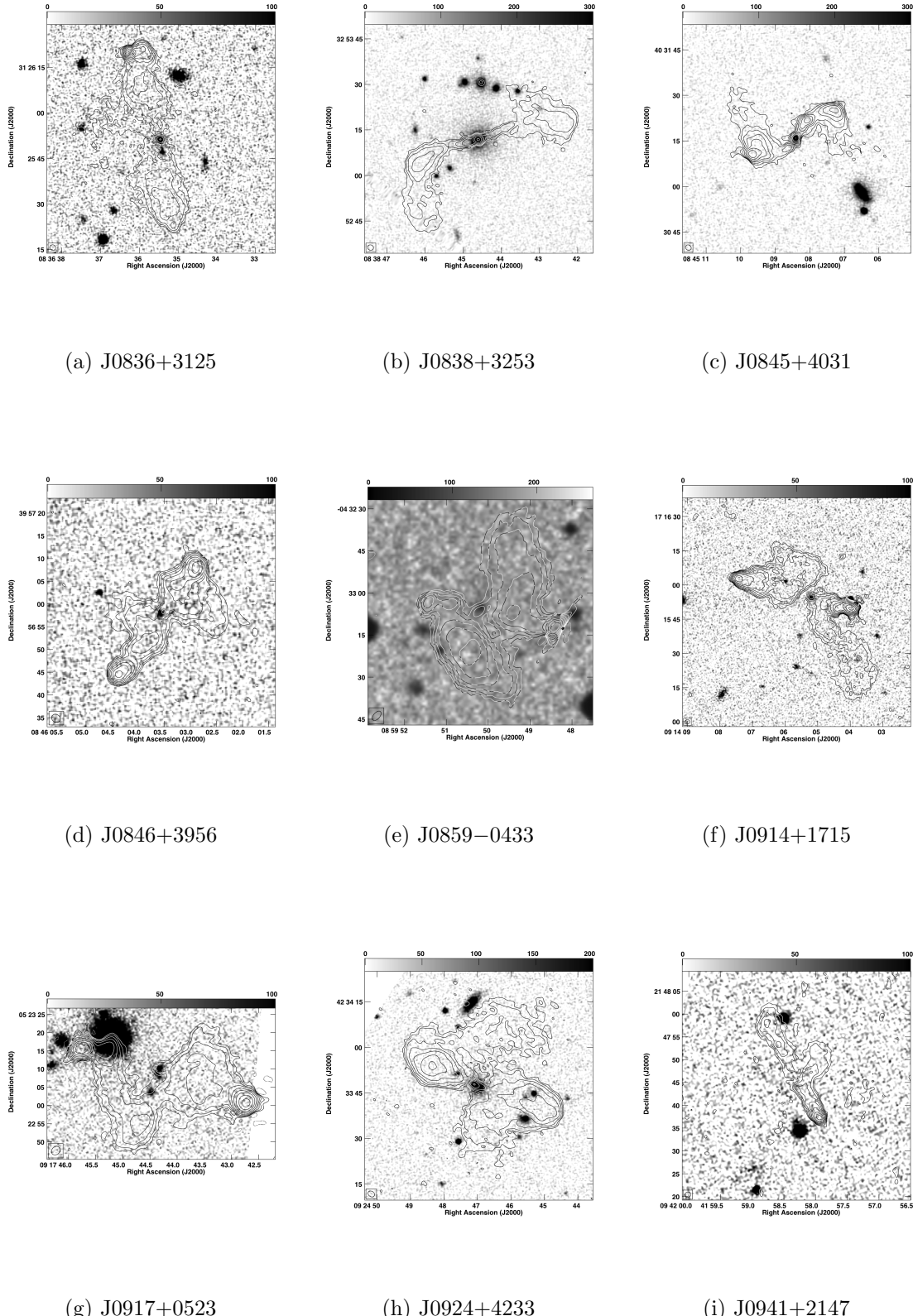


Fig. 30.— Optical overlays of a sample of 100 low axial ratio radio sources (3/11).

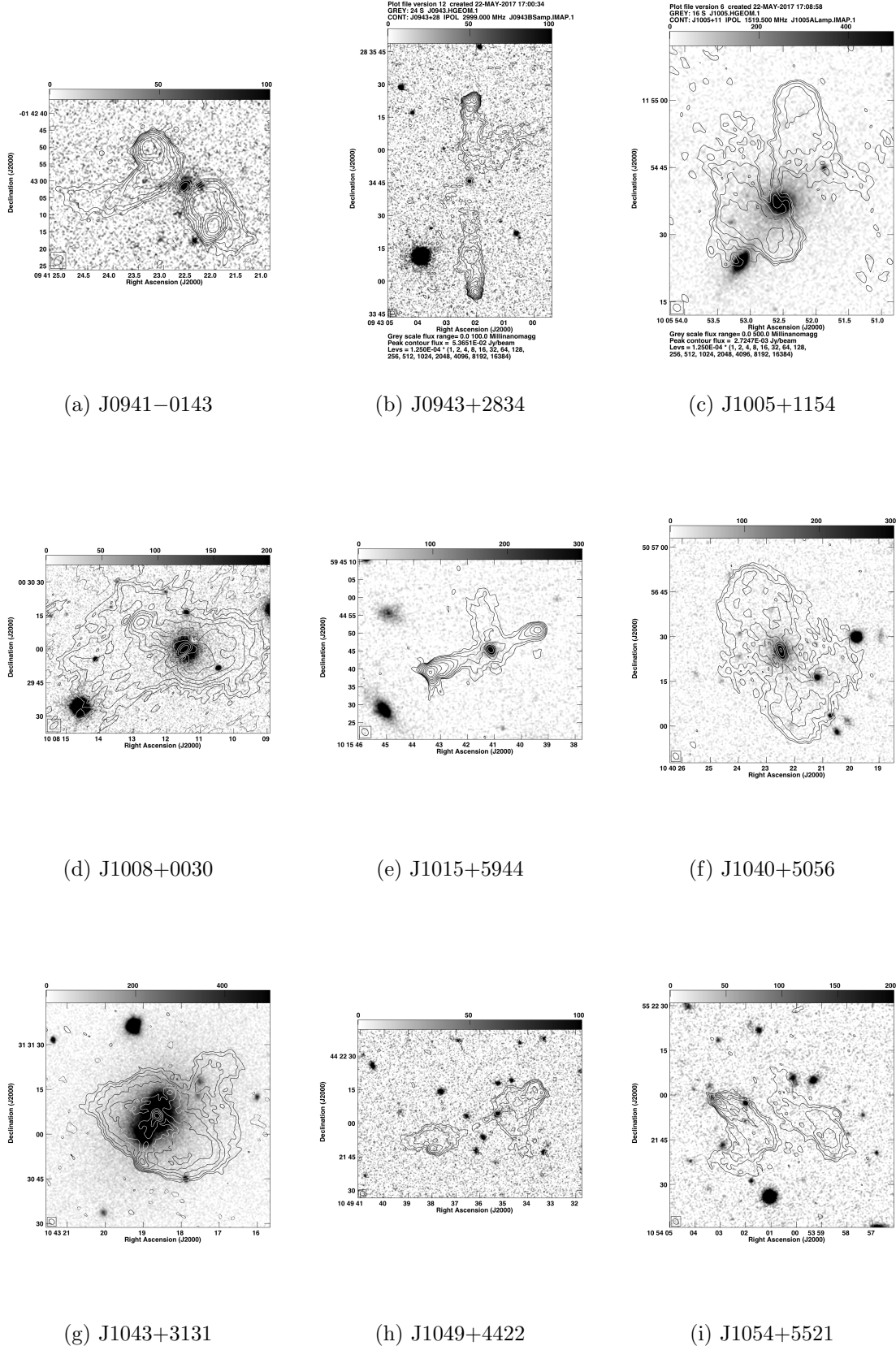


Fig. 31.—: Optical overlays of a sample of 100 low axial ratio radio sources (4/11).

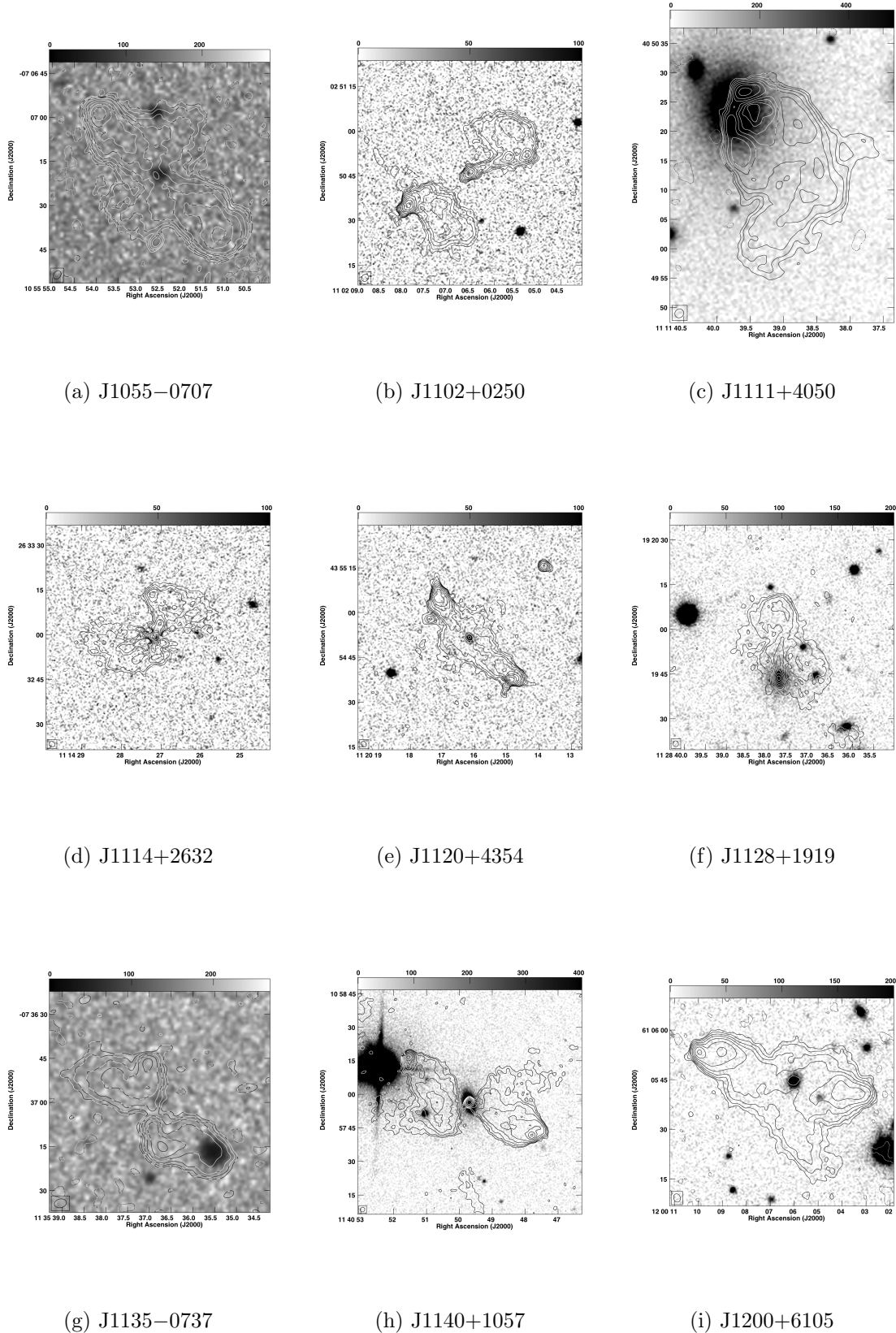


Fig. 32.—: Optical overlays of a sample of 100 low axial ratio radio sources (5/11).

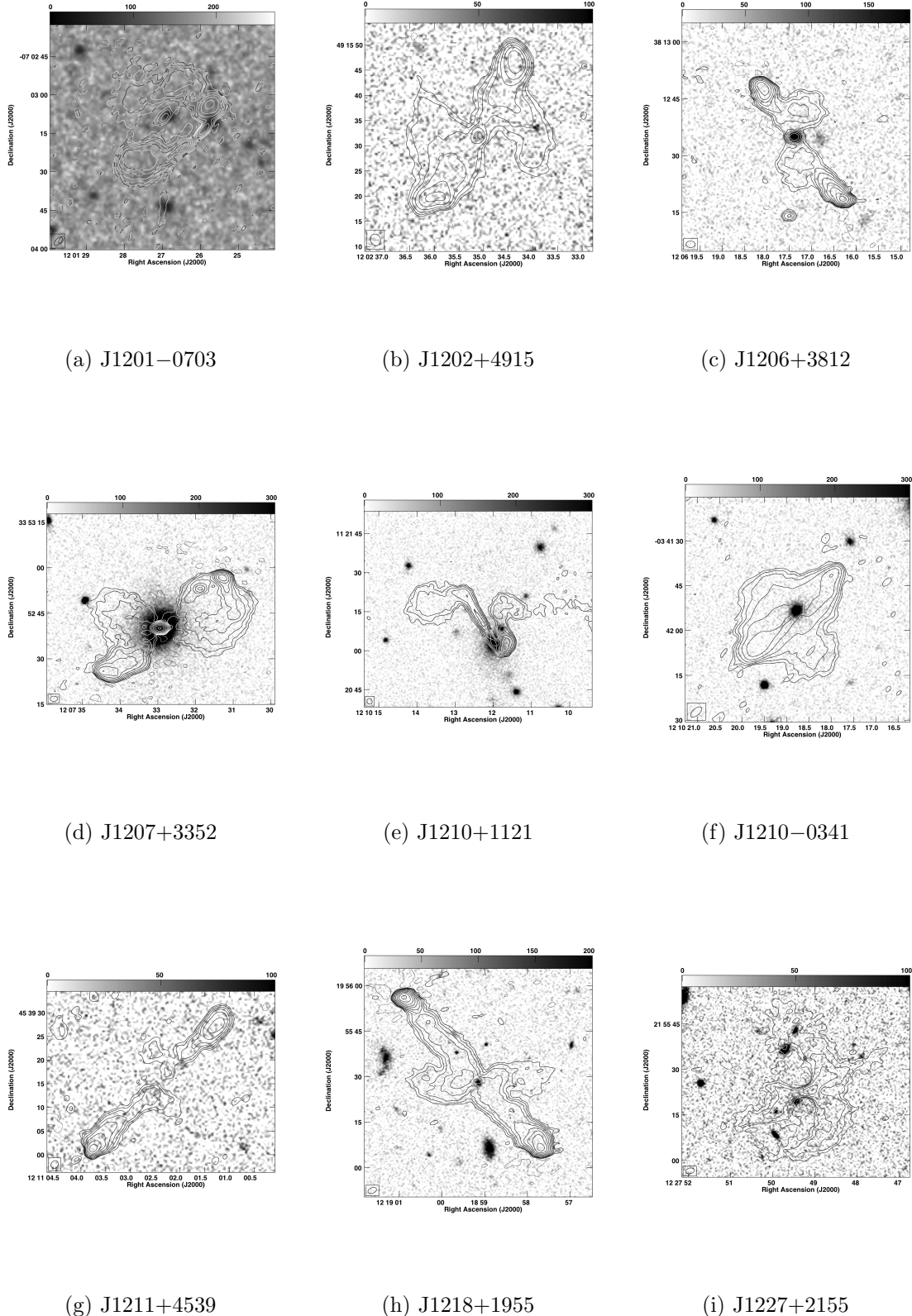


Fig. 33.— Optical overlays of a sample of 100 low axial ratio radio sources (6/11).

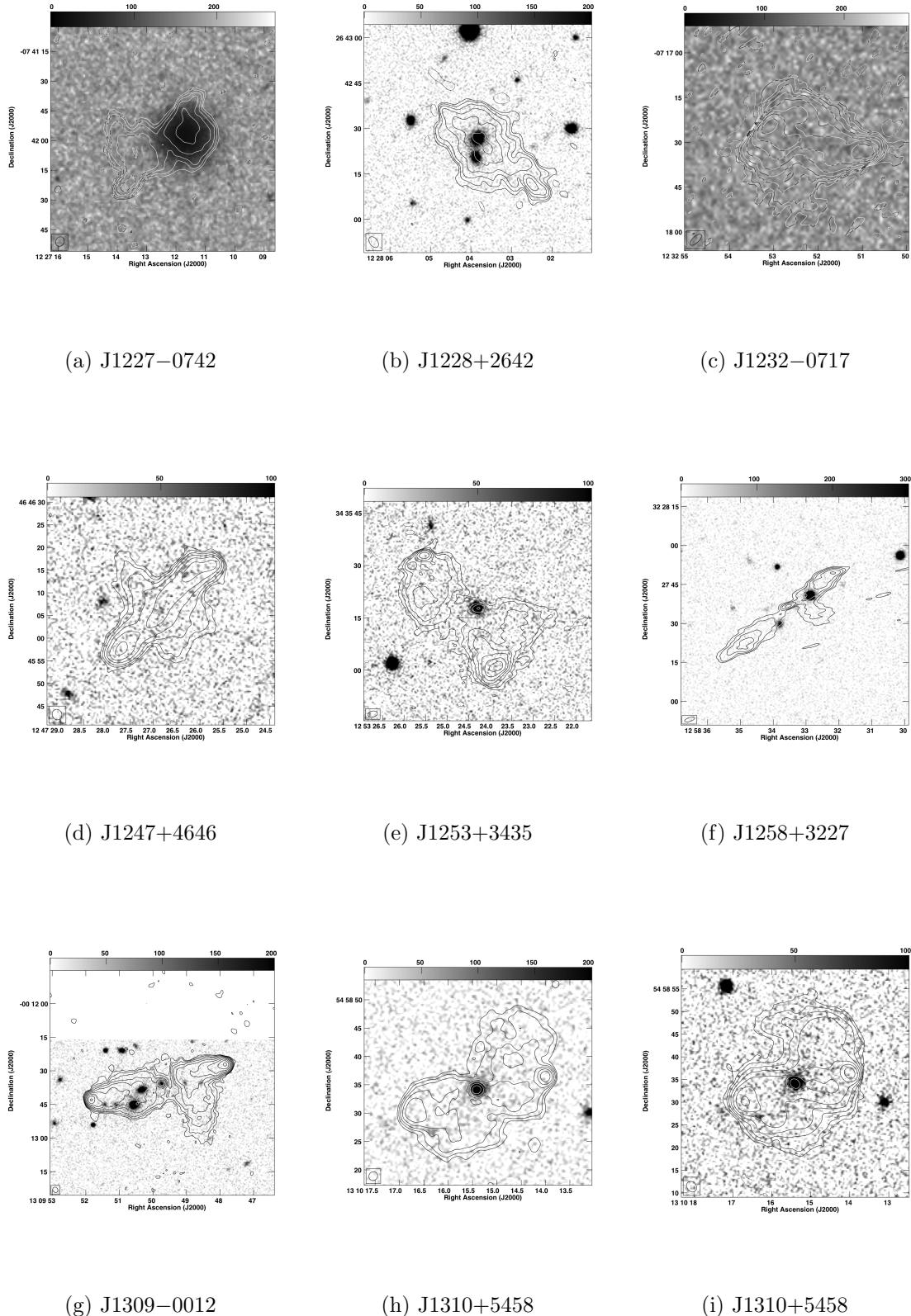


Fig. 34.—: Optical overlays of a sample of 100 low axial ratio radio sources (7/11).

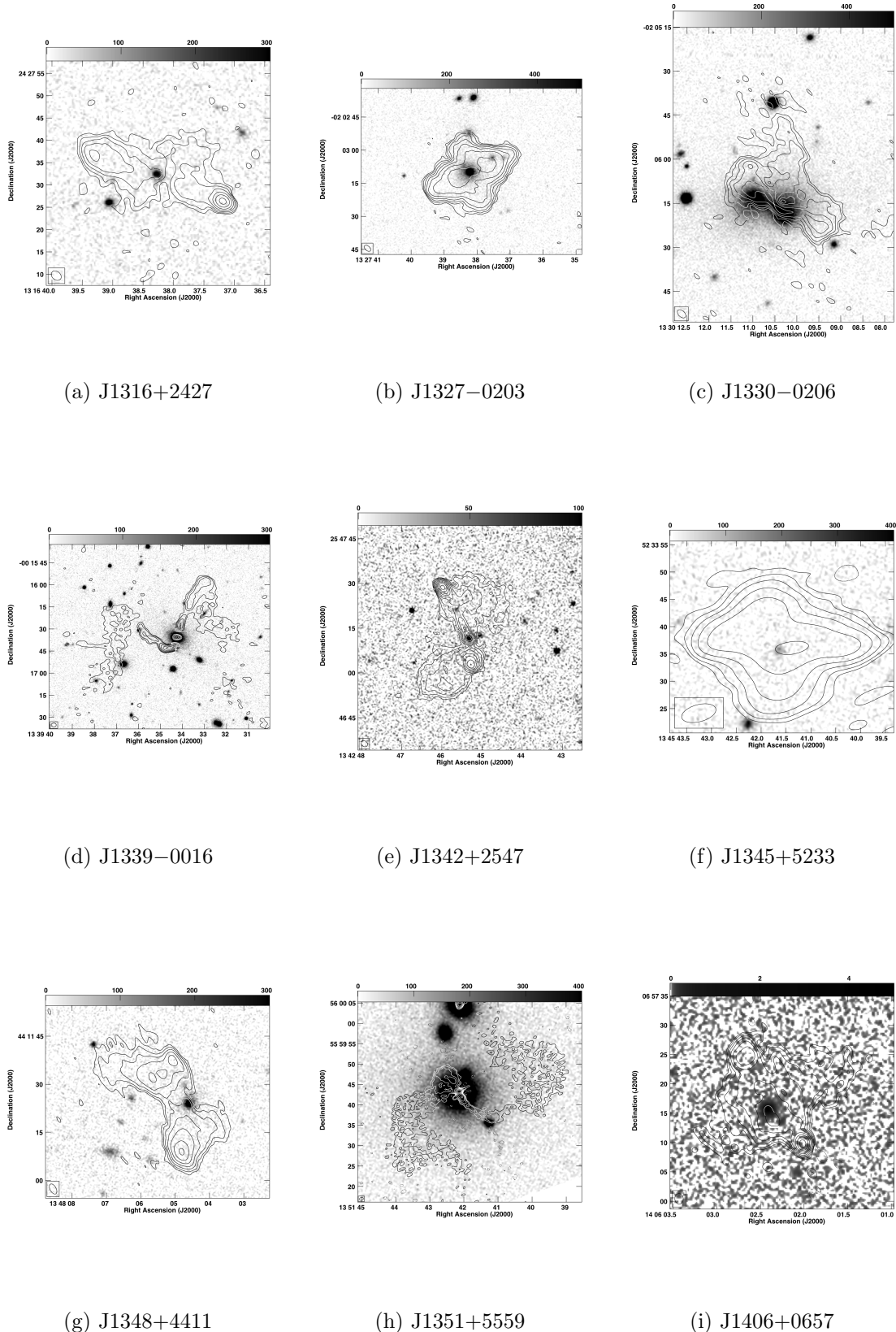


Fig. 35.— Optical overlays of a sample of 100 low axial ratio radio sources (8/11).

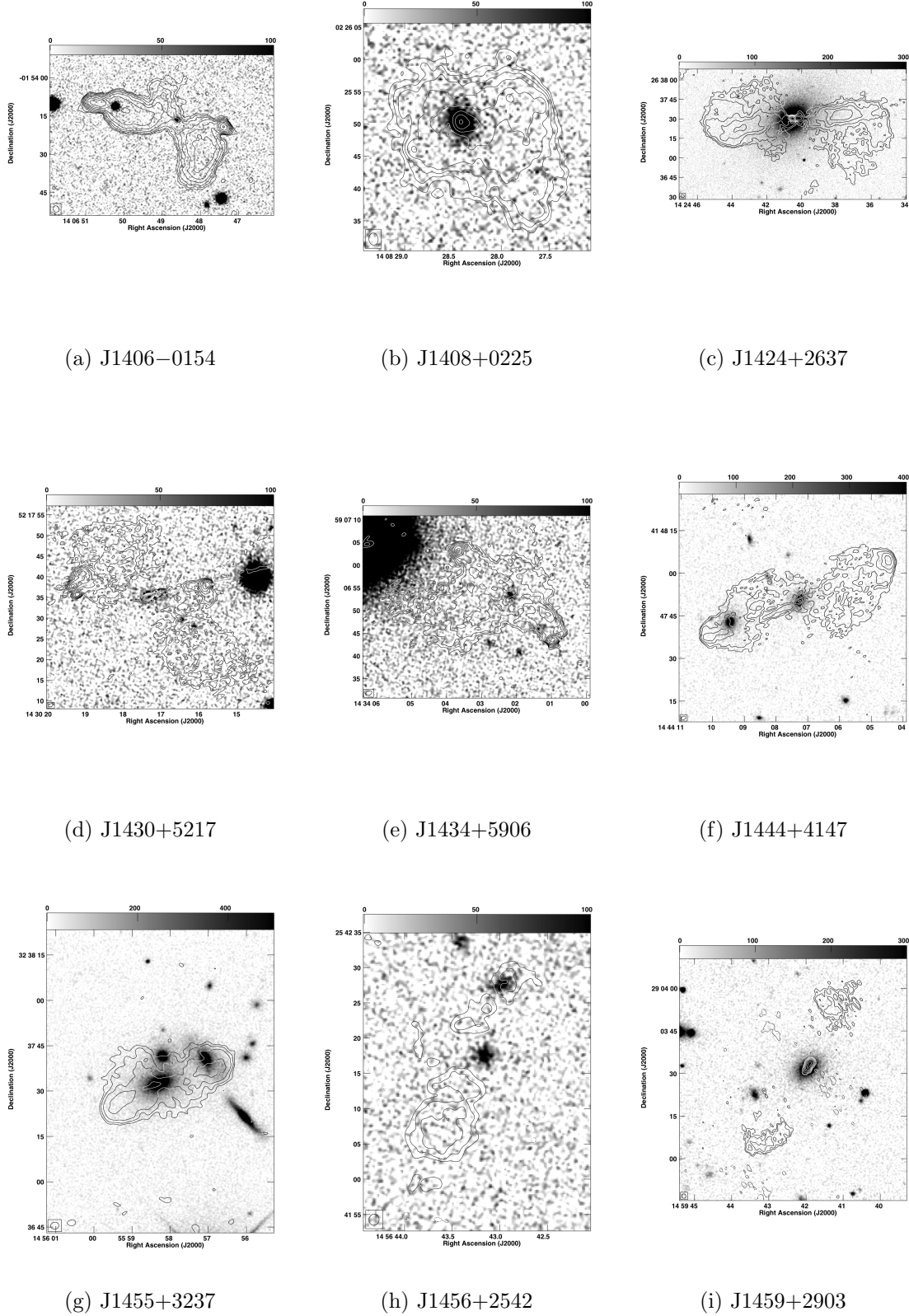


Fig. 36.—: Optical overlays of a sample of 100 low axial ratio radio sources (9/11).

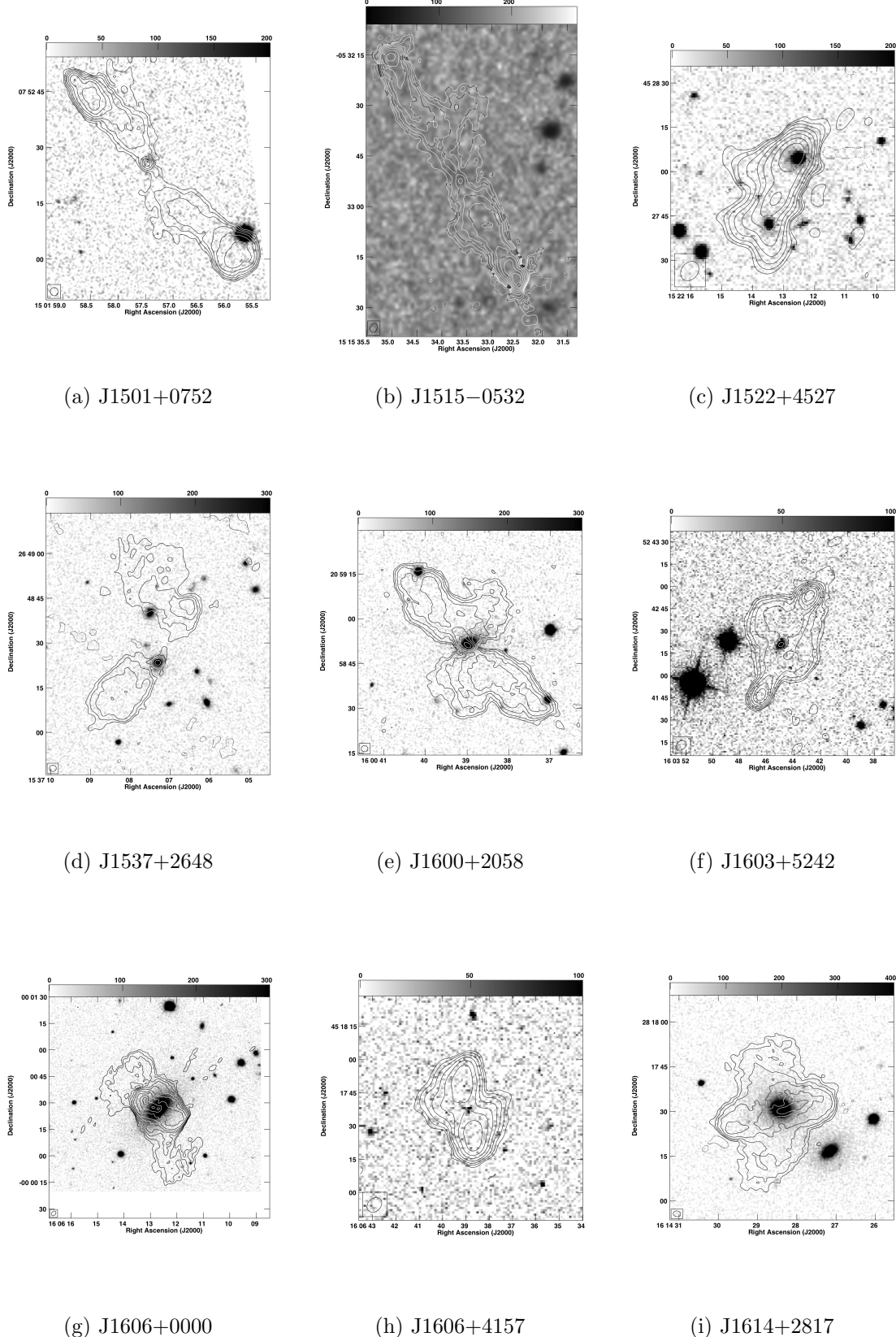


Fig. 37.—: Optical overlays of a sample of 100 low axial ratio radio sources (10/11).

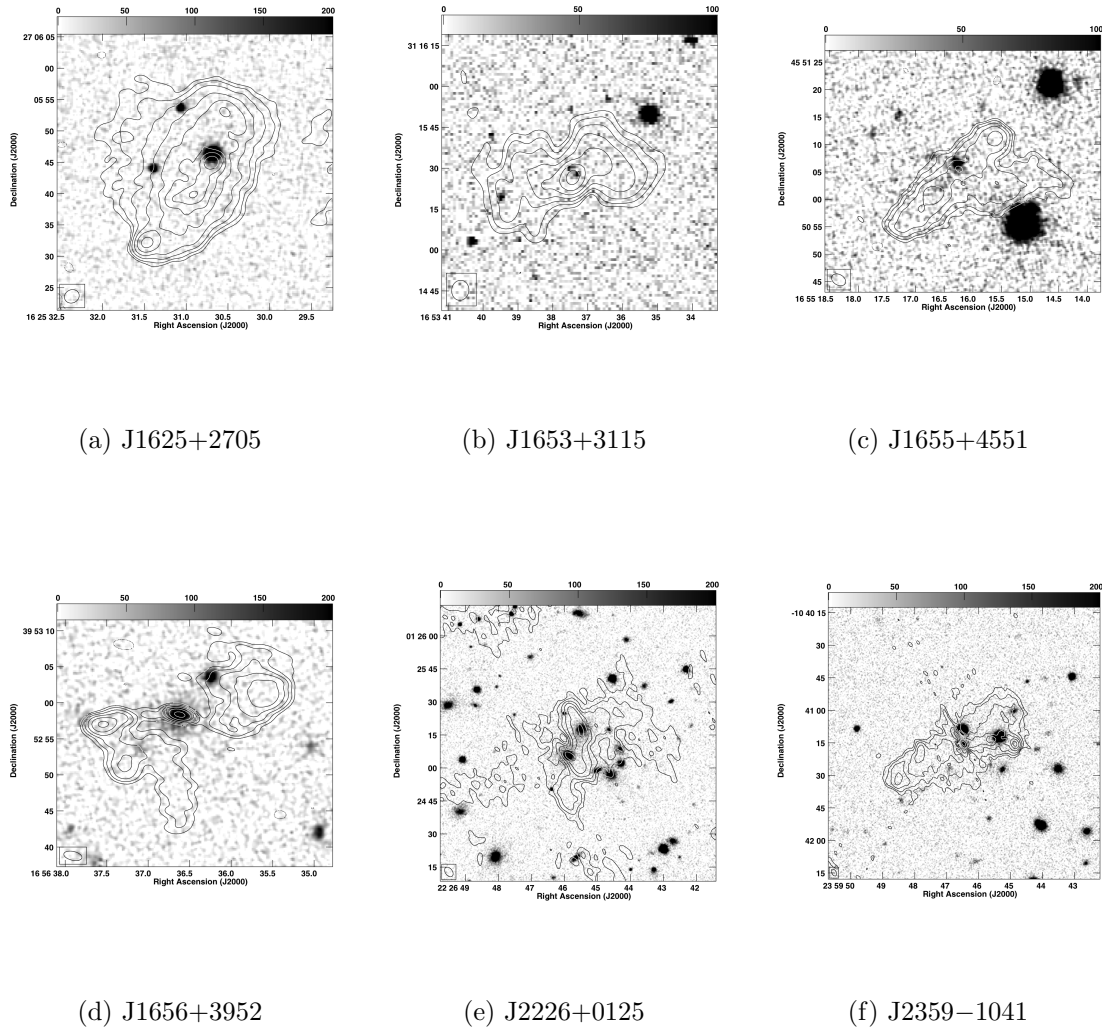


Fig. 38.—: Optical overlays of a sample of 100 low axial ratio radio sources (11/11).

REFERENCES

- Begelman, M. C., Blandford, R. D., & Rees, M. J. 1980, *Nature*, 287, 307
- Cheung, C. C. 2007, *AJ*, 133, 2097
- Harrison, R. 2014, Honors Thesis in Physics, Brandeis University.
- Merritt, D. & Ekers, R. D., 2002, *Science*, 297, 1310
- McMullin, J. P., Waters, B., Schiebel, D., Young, W., & Golap, K. 2007, Astronomical Data Analysis Software and Systems XVI (ASP Conf. Ser. 376), ed. R. A. Shaw, F. Hill, & D. J. Bell (San Francisco, CA: ASP), 127
- Rao, U., & Cornwell, T. 2011, *A&A*, 532, 71
- Roberts, D. H., Cohen, J., P., Liu, J., Saripalli, L., & Subrahmanyam, R. 2015, *ApJS*, 220, 7 (Paper I)
- Roberts, D. H. & Saripalli, L., 2017, in preparation
- Roberts, D. H., Saripalli, L., & Subrahmanyam, R. 2015, *ApL*, 810, 6
- Saripalli, L., & Roberts, D. H. 2017, *ApJ*, submitted

Table 1. Log of Observations

Source	Archival ^a Band/Array	JVLA Band/Array, Date
J0001–0033	L/A	S/C, 07feb2016; S/B, 30may2016b; L/B, 03jun2016a
J0033–0149		S/C, 07feb2016; S/B, 30may2016; L/B, 03jun2016a
J0036+0048		S/C, 07feb2016; S/B, 30may2016; L/B, 03jun2016a
J0045+0021	L/A;C/B	S/C, 07feb2016; S/B, 30may2016; L/B, 03jun2016a
J0049+0059	L/A	S/C, 07feb2016; S/B, 30may2016; L/B, 03jun2016a
J0113+0106	L/A; C/B	S/C, 07feb2016; S/B, 30may2016; L/B, 03jun2016a
J0115–0000		S/C, 07feb2016; S/B, 30may2016; L/B, 03jun2016a
J0143–0119	L/A;C/B	S/C, 04feb2016c; S/B, 30may2016a; L/B, 31may2016
J0144–0830	L/A	S/C, 04feb2016c; S/B, 30may2016a; L/B, 31may2016
J0145–0159	L/A	S/C, 04feb2016c; S/B, 30may2016a; L/B, 31may2016
J0147–0851		S/C, 04feb2016c; S/B, 30may2016a; L/B, 31may2016
J0211–0920	L/A	S/C, 04feb2016c; S/B, 30may2016a; L/B, 31may2016
J0225–0738		S/C, 04feb2016c; S/B, 30may2016a
J0702+5002	L/A	S/C, 04feb2016b; S/B, 28may2016a; L/B, 29may2016
J0725+5835		S/C, 04feb2016b; S/B, 28may2016a; L/B, 29may2016
J0805+4854		S/C, 04feb2016b; S/B, 28may2016a; L/B, 29may2016
J0813+4347	L/A	S/C, 04feb2016b; S/B, 28may2016a; L/B, 29may2016; L/A, 27dec2016
J0821+2922	L/A	S/C, 04feb2016a; S/B, 22may2016a; L/B, 28may2016b; L/A, 10jan2017
J0836+3125		S/C, 04feb2016a; S/B, 22may2016a; L/B, 28may2016b
J0838+3253		S/C, 04feb2016a; S/B, 22may2016a; L/B, 28may2016b; L/A, 10jan2017
J0845+4031	L/A	S/C, 04feb2016a; S/B, 22may2016a; L/B, 28may2016b; L/A, 27dec2016

Table 1—Continued

Source	Archival ^a Band/Array	JVLA Band/Array, Date
J0846+3956	L/A	S/C, 04feb2016a; S/B, 22may2016a; L/B, 28may2016b
J0859−0433	L/A	S/B, 03jun2016b; L/B, 14aug2016
J0914+1715		S/C, 04feb2016b; L/B, 30may2016c; S/B, 19jun2016; L/A, 10jan2017
J0917+0523	L/A	S/B, 03jun2016b; L/B, 14aug2016; L/A, 10jan2017
J0924+4233	L/A	S/C, 22apr2016; S/B, 22may2016a; L/B, 28may2016b
J0941−0143	L/A	S/B, 03jun2016b; L/B, 14aug2016
J0941+2147		S/C, 04feb2016b; L/B, 30may2016c; S/B, 19jun2016; L/A, 10jan2017
J0943+2834		S/C, 04feb2016b; L/B, 30may2016c; S/B, 19jun2016; L/A, 10jan2017
J1005+1154	L/A	S/B, 03jun2016b; L/B, 14aug2016; L/A, 10jan2017
J1008+0030	L/A	S/B, 03jun2016b; L/B, 14aug2016; L/A, 10jan2017
J1015+5944	L/A	S/C, 22apr2016; S/B, 16jul2016
J1040+5056		S/C, 22apr2016; S/B, 16jul2016
J1043+3131	L/A; C/B	S/C, 22apr2016; S/B, 16jul2016
J1049+4422		S/C, 22apr2016; S/B, 16jul2016
J1054+5521	L/A	S/C, 22apr2016; S/B, 16jul2016
J1055−0707		S/C, 29mar2016; S/B 24jul2016a;
J1102+0250		S/C, 29mar2016; S/B, 24jul2016a
J1111+4050	L/A;C/B	...
J1114+2632		S/C, 22apr2016; S/B, 16jul2016
J1120+4354		S/C, 22apr2016; S/B, 16jul2016; L/B, 26aug2016
J1128+1919		S/B, 15jun2016; L/B, 26aug2016
J1135−0737	L/A	S/C, 29mar2016; S/B, 24jul2016a

Table 1—Continued

Source	Archival ^a Band/Array	JVLA Band/Array, Date
J1140+1057		S/B, 15jun2016; L/B, 26aug2016
J1200+6105		S/B, 22may2016a; S/B, 25jun2016
J1201−0703		S/C, 29mar2016; S/B, 24jul2016a
J1202+4915	L/A	S/B, 25jun2016
J1206+3812	L/A; C/B	S/B, 22jul2016
J1207+3352	L/A;C/B	S/B, 22jul2016
J1210−0341	L/A	S/C, 29mar2016; S/B, 24jul2016a
J1210+1121		S/B, 15jun2016
J1211+4539	L/A	...
J1218+1955		S/B, 22jul2016
J1227−0742	L/A	S/C, 29mar2016; S/B, 24jul2016a
J1227+2155	L/A	S/C, 29mar2016; S/B, 22jul2016
J1228+2642	L/A	S/B, 22jul2016
J1232−0717		S/C, 29mar2016; S/B, 24jul2016a
J1247+4646		S/B, 25jun2016
J1253+3435	L/A	S/B, 22jul2016
J1258+3227		S/B, 22jul2016
J1309-0012	C/B	S/B, 24jul2016b
J1310+5458	L/A	S/B, 25jun2016
J1316+2427		S/B, 24jul2016b
J1327−0203	L/A	S/B, 24jul2016b
J1330−0206		S/B, 24jul2016b

Table 1—Continued

Source	Archival ^a Band/Array	JVLA Band/Array, Date
J1339–0016		S/B, 24jul2016b
J1342+2547	L/A	S/B, 24jul2016b
J1345+5233	L/A	S/C, 30mar2016a; S/AB, 25sep2016
J1348+4411	L/A	S/C, 30mar2016a; S/AB, 25sep2016
J1351+5559		S/C, 30mar2016a; S/AB, 25sep2016
J1353+0724		...
J1406–0154	L/A	S/B, 24jul2016b
J1406+0657	L/A	...
J1408+0225	L/A	...
J1411+0907		...
J1424+2637		S/B, 24jul2016b
J1430+5217	L/A	S/C, 30mar2016a; S/AB, 25sep2016
J1433+0037		...
J1434+5906	L/A	S/C, 30mar2016a; S/AB, 25sep2016
J1437+0834		...
J1444+4147		S/C, 30mar2016a
J1454+2732		...
J1455+3237		S/B, 24jul2016b
J1456+2542	L/A	...
J1459+2903	L/A; C/B	...
J1501+0752		S/B, 05aug2016
J1515+0532		S/B, 05aug2016

Table 1—Continued

Source	Archival ^a Band/Array	JVLA Band/Array, Date
J1522+4527		S/C, 30mar2016a
J1537+2648		S/C, 30mar2016b; S/B, 05aug2016
J1600+2058	L/A	S/C, 30mar2016b; S/B, 05aug2016
J1603+5242		S/C, 30mar2016b
J1606+0000	L/A	S/B, 05aug2016
J1606+4517	L/A	S/C, 30mar2016b
J1614+2817	L/A	S/B, 05aug2016
J1625+2705	L/A	S/B, 05aug2016
J1653+3115		S/C, 30mar2016b
J1655+4551		S/C, 30mar2016b; S/B, 05aug2016
J1656+3952	L/A	S/C, 30mar2016b
J2226+0125		S/C, 04Feb2016; S/B, 30may2016a; L/B, 31may2016
J2359−1041		S/C, 07feb2016; S/B, 30may2016; L/B, 03jun2016a

^aRoberts et al. 2015.

Table 2. Figure Properties

Source IAU Name	Figure Number	A-Array L-band ^a Low, Peak (mJy/beam)	B-Array C-band ^a Low, Peak (mJy/beam)	AB-Array S-band Low, Peak (mJy/beam)	B-Array L-band Low, Peak (mJy/beam)	B-Array S-band Low, Peak (mJy/beam)	C-Array S-band Low, Peak (mJy/beam)
J0001–0033	1 (a–d)	0.10, 2.37	0.18, 6.82	0.09, 2.23	0.10, 10.2
J0033–0149	1 (e–g)	0.18, 10.1	0.09, 3.72	0.09, 11.5
J0036+0048	1 (h&i)	0.18, 65.8	0.09, 25.1	...
J0045+0021	2 (a–d)	0.30, 178	0.50, 60.8	...	0.18, 249	0.18, 109	...
J0049+0059	2 (e–h)	0.09, 2.51	0.18, 9.60	0.09, 2.64	0.10, 12.9
J0113+0106	2 (i), 3 (a–c)	0.70, 18	0.18, 12.5	0.09, 4.32	0.14, 16.4
J0115–0000	3 (d–f)	0.25, 15.2	0.09, 4.99	0.14, 15.6
J0143–0119	3 (g–i), 4 (a&b)	0.20, 44.4	0.09, 34.0	...	0.28, 80.5	0.09, 47.0	0.16, 110
J0144–0830	4 (c–f)	0.09, 1.40	0.20, 7.25	0.09, 1.69	0.16, 5.88
J0145–0159	4 (g–i), 5 (a)	0.20, 2.56	0.25, 9.45	0.09, 3.02	0.20, 18.7
J0147–0851	5 (b–d)	0.18, 33.2	0.09, 14.4	0.16, 30.2
J0211–0920	5 (e–h)	0.10, 2.81	0.18, 10.6	0.09, 2.65	0.13, 14.4
J0225–0738	5 (i), 6 (a&b)	0.20, 51.4	0.09, 18.3	0.18, 49.1
J0702+5002	6 (c–f)	0.22, 5.74	0.18, 28.4	0.07, 4.88	0.09, 21.7
J0725+5835	6 (g–i), 7 (a)	0.22, 4.11	0.18, 10.0	0.07, 2.77	0.09, 8.19
J0805+4854	7 (b–d)	0.18, 11.5	0.10, 4.38	0.06, 5.86
J0813+4347	7 (e–h)	0.14, 9.91	0.18, 22.1	0.07, 9.93	0.09, 17.1
J0821+2922	7 (i), 8 (a–c)	0.16, 1.93	0.17, 9.40	0.06, 1.98	0.09, 13.8
J0836+3125	8 (d–g)	0.16, 41.1	0.28, 60.0	0.09, 30.5	0.09, 53.5
J0838+3253	8 (h&i), 9 (a&b)	0.13, 5.52	0.20, 6.89	0.09, 6.54	0.09, 10.6
J0845+4031	9 (c–f)	0.20, 15.5	0.20, 31.7	0.09, 11.1	0.09, 32.3
J0846+3956	9 (g–i), 10 (a)	0.18, 16.1	0.20, 33.0	0.06, 11.1	0.09, 33.1
J0859–0433	10 (b–d)	0.20, 23.4	0.20, 26.8	0.07, 16.0	...
J0914+1715	10 (e–h)	0.31, 157	0.35, 586	0.13, 160	0.18, 335
J0917+0523	10 (i), 11 (a&b)	0.28, 96.6	0.35, 165	0.14, 74.2	...
J0924+4233	11 (c–f)	0.28, 6.24	0.17, 43.8	0.09, 4.74	0.10, 29.2
J0941–0143	11 (g–i)	0.60, 76.9	0.35, 188	0.14, 68.2	...
J0941+2147	12 (a–d)	0.28, 54	0.25, 79.6	0.09, 39.5	0.13, 56.5
J0943+2834	12 (e–h)	0.20, 62.5	0.50, 142	0.13, 53.7	0.13, 91.3
J1005+1154	12 (i), 13 (a&b)	0.20, 2.72	0.28, 16.8	0.07, 3.57	...
J1008+0030	13 (c–e)	0.20, 66.1	0.35, 75.2	0.08, 75.2	...
J1015+5944	13 (f–h)	0.20, 98.1	0.09, 49.3	0.10, 86.7

Table 2—Continued

Source IAU Name	Figure Number	A-Array L-band ^a Low, Peak (mJy/beam)	B-Array C-band ^a Low, Peak (mJy/beam)	AB-Array S-band Low, Peak (mJy/beam)	B-Array L-band Low, Peak (mJy/beam)	B-Array S-band Low, Peak (mJy/beam)	C-Array S-band Low, Peak (mJy/beam)
J1040+5056	13 (i), 14 (a)	0.06, 2.20	0.07, 7.63
J1043+3131	14 (b–e)	0.40, 44.6	0.08, 36.2	0.09, 37.8	0.10, 68.0
J1049+4422	14 (f&g)	0.09, 4.50	0.10, 21.4
J1054+5521	14 (h&i), 15 (a)	0.18, 14.1	0.09, 9.40	0.10, 21.5
J1055–0707	15 (b&c)	0.09, 16.6	0.10, 42.9
J1102+0250	15 (d&e)	0.13, 83.0	0.10, 96.4
J1111+4050	15 (f)	...	0.13, 11.3
J1114+2632	15 (g&h)	0.09, 26.8	0.07, 62.0
J1120+4354	15 (i), 16 (a)	0.09, 38.2	0.10, 71.0
J1128+1919	16 (b&c)	0.25, 19.8	0.09, 15.1	...
J1135–0737	16 (d–f)	0.20, 2.00	0.09, 3.86	0.07, 7.39
J1140+1057	16 (g&h)	0.25, 32.3	0.09, 14.0	...
J1200+6105	16 (i)	0.05, 7.61	...
J1201–0703	17 (a&b)	0.10, 8.29	0.10, 19.8
J1202+4915	17 (c&d)	0.15, 7.97	0.05, 7.34	...
J1206+3812	17 (e–g)	0.20, 47.0	0.15, 23.1	0.07, 24.7	...
J1207+3352	17 (h)	0.07, 51.6	...
J1210–0341	17 (i), 18 (a&b)	0.10, 2.95	0.09, 5.28	0.07, 16.5
J1210+1121	18 (c&d)	0.20, 17.3	0.09, 4.57	...
J1211+4539	18 (e)	0.20, 43.6
J1218+1955	18 (f)	0.14, 88.4	...
J1227–0742	18 (g–i)	0.18, 0.86	0.13, 3.12	0.09, 7.47
J1227+2155	19 (a&b)	0.18, 3.74	0.10, 2.91	...
J1228+2642	19 (c&d)	0.08, 4.35	0.10, 5.66	...
J1232–0717	19 (e&f)	0.10, 19.0	0.10, 53.4
J1247+4646	19 (g)	0.07, 3.23	...
J1253+3435	19 (h&i)	0.09, 17.0	0.14, 13.8	...
J1258+3227	20 (a)	0.14, 120	...
J1309-0012	20 (b&c)	...	0.30, 113	0.20, 60.1	...
J1310+5458	20 (d&e)	0.20, 11.3	0.07, 7.72	...
J1316+2427	20 (f)	0.10, 10.5	...
J1327–0203	20 (g&h)	0.20, 20.9	0.20, 23.6	...
J1330–0206	20 (i)	0.10, 3.34	...

Table 2—Continued

Source IAU Name	Figure Number	A-Array L-band ^a Low, Peak (mJy/beam)	B-Array C-band ^a Low, Peak (mJy/beam)	AB-Array S-band Low, Peak (mJy/beam)	B-Array L-band Low, Peak (mJy/beam)	B-Array S-band Low, Peak (mJy/beam)	C-Array S-band Low, Peak (mJy/beam)
J1339–0016	21 (a)	0.14, 6.48	...
J1342+2547	21 (b&c)	0.30, 76.4	0.09, 29.9	...
J1345+5233	21 (d–f)	0.09, 0.92	...	0.07, 2.47	0.18, 8.74
J1348+4411	21 (g–i)	0.07, 5.96	...	0.06, 4.59	0.07, 24.0
J1351+5559	22 (a&b)	0.04, 4.61	0.07, 17.4
J1406–0154	22 (c&d)	0.30, 57.6	0.09, 24.2	...
J1406+0657	22 (e)	0.20, 71.4
J1408+0225	22 (f)	0.10, 13.9
J1424+2637	22 (g)	0.09, 9.05	...
J1430+5217	22 (h&i), 23 (a)	0.20, 40.2	...	0.08, 12.4	0.14, 80.8
J1434+5906	23 (b–d)	0.15, 47.3	...	0.06, 23.4	0.14, 41.2
J1444+4147	23 (e&f)	0.10, 2.15	0.14, 17.9
J1455+3237	23 (g)	0.06, 1.16	...
J1456+2542	23 (h)	0.11, 1.18
J1459+2903	23 (i), 24 (a)	0.20, 8.67	0.10, 10.1
J1501+0752	24 (b)	0.07, 14.0	...
J1515+0532	24 (c)	0.15, 70.3	...
J1522+4527	24 (d)	0.07, 17.3
J1537+2648	24 (e&f)	0.15, 3.57	0.10, 16.8
J1600+2058	24 (g–i)	0.20, 6.89	0.10, 8.72	0.10, 21.3
J1603+5242	25 (a)	0.20, 42.7
J1606+0000	25 (b&c)	0.20, 82.8	0.25, 80.5	...
J1606+4517	25 (d&e)	0.20, 3.22	0.10, 11.1
J1614+2817	25 (f&g)	0.20, 8.07	0.14, 8.55	...
J1625+2705	25 (h&i)	0.70, 2.80	0.20, 41.8	...
J1653+3115	26 (a)	0.40, 74.1
J1655+4551	26 (b&c)	0.10, 5.30	0.14, 16.7
J1656+3952	26 (d&e)	0.20, 8.06	0.07, 20.8
J2226+0125	26 (f–h)	0.28, 10.9	0.09, 4.12	0.20, 8.79
J2359–1041	26 (i), 27 (a&b)	0.25, 12.3	0.13, 11.2	0.14, 18.8

^aRoberts et al. 2015.